A Slowly Precessing Disk in the Nucleus of M31 as the Feeding Mechanism for a Central Starburst

K. E. Lockhart[1] , J. R. Lu[2] , H. V. Peiris[3,4] , R. M. Rich[5], A. Bouchez[6], and A. M. Ghez[5]
[1] Institute for Astronomy, University of Hawaii, Manoa, Honolulu, HI 96822, USA
[2] Department of Astronomy, University of California, Berkeley, CA 94720, USA; jlu.astro@berkeley.edu
[3] Department of Physics and Astronomy, University College London, London WC1E 6BT, UK
[4] The Oskar Klein Centre for Cosmoparticle Physics, Stockholm University, AlbaNova, Stockholm, SE-106 91, Sweden
[5] Department of Physics and Astronomy, University of California, Los Angeles, CA 90095, USA
[6] Giant Magellan Telescope, Pasadena, CA 91107, USA

Abstract

We present a kinematic study of the nuclear stellar disk in M31 at infrared wavelengths using high spatial resolution integral field spectroscopy. The spatial resolution achieved, FWHM = $0.''12$ (0.45 pc at the distance of M31), has only previously been equaled in spectroscopic studies by space-based long-slit observations. Using adaptive-optics-corrected integral field spectroscopy from the OSIRIS instrument at the W. M. Keck Observatory, we map the line-of-sight kinematics over the entire old stellar eccentric disk orbiting the supermassive black hole (SMBH) at a distance of $r < 4$ pc. The peak velocity dispersion is 381 ± 55 km s^{-1}, offset by $0.''13 \pm 0.''03$ from the SMBH, consistent with previous high-resolution long-slit observations. There is a lack of near-infrared (NIR) emission at the position of the SMBH and young nuclear cluster, suggesting a spatial separation between the young and old stellar populations within the nucleus. We compare the observed kinematics with dynamical models from Peiris & Tremaine. The best-fit disk orientation to the NIR flux is $[\theta_l, \theta_i, \theta_a] = [-33° \pm 4°, 44° \pm 2°, -15° \pm 15°]$, which is tilted with respect to both the larger-scale galactic disk and the best-fit orientation derived from optical observations. The precession rate of the old disk is $\Omega_P = 0.0 \pm 3.9$ km s^{-1} pc^{-1}, lower than the majority of previous observations. This slow precession rate suggests that stellar winds from the disk will collide and shock, driving rapid gas inflows and fueling an episodic central starburst as suggested in Chang et al.

Key words: black hole physics – galaxies: kinematics and dynamics – galaxies: nuclei – infrared: stars – stars: kinematics and dynamics

1. Introduction

Many galaxies harbor not only supermassive black holes (SMBH) but also young stellar populations in the central few parsecs. The origin of these young stars is unusual given that extreme tidal forces near the SMBH will shear typical molecular clouds apart before they can collapse to form stars (e.g., Sanders 1992; Morris 1993). A young or intermediate-age stellar population has been detected in nearly all nuclear star clusters found in nearby galaxies (Allen et al. 1990; Paumard et al. 2006; Rossa et al. 2006; Seth et al. 2006), including in the nuclear star cluster of M31. The SMBH in M31 (distance $d = 785$ pc, black hole mass $M_\bullet \sim 10^8 \, M_\odot$; McConnachie et al. 2005; Bender et al. 2005) is surrounded by a young (<200 Myr) nuclear cluster designated P3, which is visible in the ultraviolet (UV), has a total mass of $\sim 10^4 \, M_\odot$, is confined to the central $0.''1$ (0.4 pc), and is orbiting in a disk coplanar with the rest of the nuclear star cluster (e.g., Lauer et al. 1998; Bender et al. 2005; Lauer et al. 2012). The abundance of young stars around nearby SMBHs suggests that whatever physical mechanism deposits or forms stars in this region may be important in many galactic nuclei.

One explanation for the existence of young stars near an SMBH is in situ star formation in a massive self-gravitating gas disk around the SMBH, such as has been postulated for the Milky Way from kinematic studies of its young stellar population (Levin & Beloborodov 2003; Lu et al. 2009; Yelda et al. 2014). Such a disk would be sufficiently dense to overcome the strong tidal forces and fragment to form stars, as has been suggested in the context of active galactic nucleus

(AGN) accretion disks (e.g., Kolykhalov & Syunyaev 1980; Goodman 2003). Unlike the Milky Way, which hosts $\geqslant 10^4 \, M_\odot$ of cold gas and dust in the inner 5 pc (Genzel et al. 1985), M31 is relatively gas-poor in the central few kiloparsecs (Sofue & Yoshida 1993; Nieten et al. 2006), and the origin of the gas that formed the young nuclear star cluster is not yet known.

In M31, there is an eccentric disk of old stars extending a few parsecs from the central SMBH (Tremaine 1995) that has been postulated to be both the source of the molecular gas and the means for ushering that gas into the central parsec, where the young stars are observed (Chang et al. 2007). The mass loss from the red giants and asymptotic giant branch stars in this disk is high enough to drive a new in situ star formation event every 500 Myr, if there are crossing orbits in the eccentric disk of old stars. The crossing orbits would lead to gas collisions, shocks, and inflows on timescales shorter than typical viscous times. The presence of such crossing orbits depends critically on a low precession speed ($\lesssim 10$ km s^{-1} pc^{-1}) for the eccentric disk of old stars.

The structure and kinematics of the eccentric nuclear disk have been studied at multiple wavelengths. Optical high spatial resolution observations with the *Hubble Space Telescope* (*HST*; Lauer et al. 1993, 1998) reveal the structure of the eccentric disk: a brighter stellar concentration, P1, at apoapse and a fainter concentration, P2, at periapse. The old stellar disk surrounds the young nuclear cluster, P3, and extends roughly $1''$ (4 pc) from the SMBH (Figure 1). The red color of the disk suggests an older stellar population, assumed to be roughly the age of the surrounding bulge, or >4 Gyr (Olsen et al. 2006;
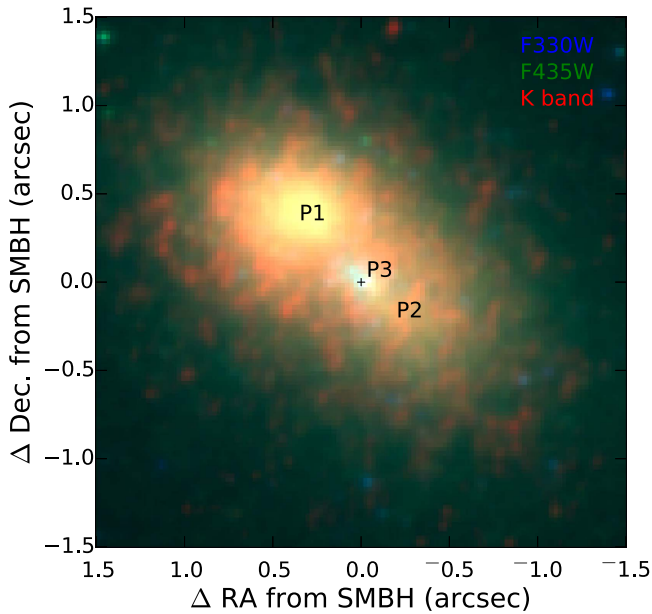
Figure 1. Three-color image of the nucleus of M31 with components labeled. The eccentric disk is demarcated by P1 at apoapse and P2 at periapse and contains old stars. The young nuclear cluster, P3, is centered on the SMBH and is prominent at blue wavelengths. $1''$ is ~ 4 pc at M31's distance of 785 pc.

Saglia et al. 2010). Current dynamical models (Peiris & Tremaine 2003) suggest that the orientation of the eccentric disk is inclined $\sim 20°$ to the larger-scale galactic disk. CO observations with the HEterodyne Receiver Array (HERA) on the IRAM 30 m telescope show that a dusty 0.7 kpc ring is also misaligned with the larger-scale galactic disk, with a position angle (P.A.) of $-66°$ versus $37°$ for the larger disk (Melchior & Combes 2013), which is not aligned with the eccentric nuclear disk. Recent dynamical models of the eccentric nuclear disk also show that it is thick ($h/r \sim 0.4$; Peiris & Tremaine 2003) and that the razor-thin models (Sambhus & Sridhar 2000; Jacobs & Sellwood 2001; Salow & Statler 2001; Sambhus & Sridhar 2002; Salow & Statler 2004) cannot properly fit the observations.

A wide range of conflicting precession values, Ω_P, have been measured for the eccentric disk, from 3 to over 30 km s^{-1} pc^{-1} (Sambhus & Sridhar 2000; Bacon et al. 2001; Jacobs & Sellwood 2001; Salow & Statler 2001; Sambhus & Sridhar 2002; Salow & Statler 2004). Thus, the origin of the gas that formed P3 remains unresolved. The existence of the eccentric disk also poses another puzzle: realistic models that explain its existence are difficult to compute. Simulations suggest that gas inflows can drive large-scale gas instabilities that can set up long-lived nuclear eccentric disks (Hopkins & Quataert 2010), or that a pair of counterrotating massive star clusters can decompose into an eccentric disk (Kazandjian & Touma 2013). Either method predicts that the resulting structure will be slowly precessing ($\Omega_P = 1$–5 km s^{-1} pc^{-1}). However, the issue is by no means settled observationally or theoretically.

Complete modeling of the eccentric disk, including a precise measurement of the precession rate, has been limited by the fact that many spectroscopic studies of the eccentric disk have used long-slit spectroscopy, often in combination with imaging (Kormendy & Bender 1999; Statler et al. 1999; Bender et al. 2005). While several of these long-slit studies have been at high spatial resolution ($\lesssim 0''1$), they have been limited by

lack of coverage of the field of view (FOV). Several integral field spectroscopy studies have been conducted (Bacon et al. 2001; Menezes et al. 2013), but the limited spatial resolution ($\sim 0''4$) likely contributes to some of the scatter in the precession rate measurements. In addition, all spectroscopic studies of the eccentric disk to date have been conducted in the optical, though the eccentric disk is brighter in the near-infrared (NIR). With the advent of laser guide star adaptive optics (LGS AO) feeding integral field unit (IFU) spectrographs, high spatial resolution 2D kinematics can now be obtained and used to test precessing eccentric disk models and hypotheses for the formation of the young nuclear star cluster in M31.

We present new observations of the nucleus of M31 obtained with the OSIRIS IFU spectrograph and the LGS AO system at the Keck Observatory. With a spatial resolution of $0''13$ (0.45 pc), we map the line-of-sight kinematics over the entire old stellar eccentric disk. We model the observed 2D flux, velocity, and dispersion maps with dynamical models from Peiris & Tremaine (2003), adding rigid-body precession to the model. The measured slow precession rate supports the Chang et al. (2007) theory for the formation of the young nuclear cluster from the winds of the old eccentric disk. We discuss the observations in Section 2, including new ground-based NIR data in Section 2.1, the data reduction and analysis in Section 3, and results from the data in Section 4. The results from the analysis are compared to models in Section 5 and discussed in Section 6. We summarize our conclusions in Section 7.

2. Observations

New high spatial resolution observations of the nucleus of M31 ($\alpha = 00\ 42\ 44.3$, $\delta = +41\ 16\ 09$, J2000) were taken in the NIR with the adaptive optics system at the W. M. Keck Observatory. Archival optical *HST* imaging was obtained to place the new NIR observations in context. While *HST* provides high-resolution imaging in the optical, the only means of obtaining high spatial resolution integral field spectroscopy is using ground-based adaptive optics (AO) in the IR. Details of the AO-assisted infrared integral field spectroscopy and imaging are described in Section 2.1. Optical imaging with *HST* is described in Section 2.2.

2.1. Ground-based Observations

NIR observations of the nucleus of M31 were taken with the LGS AO system on the W. M. Keck II 10 m telescope (van Dam et al. 2006; Wizinowich et al. 2006). The laser was positioned on the nucleus to correct high-order atmospheric aberrations. Low-order aberrations were corrected using two different tip-tilt stars during different observing runs. During good seeing, a close and faint globular cluster was used for tip-tilt correction; it is located $35''$ to the southwest from the nucleus with $R = 16.2$ at 00 42 42.203 + 41 15 46.01 (J2000). A second globular cluster, NB95, with $R = 14.9$ and located $53''$ southeast from the nucleus at 00 42 47.973 + 41 15 37.07, was used as the tip-tilt reference when seeing was poor or variable or if clouds were present (Battistini et al. 1993; Galleti et al. 2007). These tip-tilt objects are located in a region of M31 with high surface brightness and a strong gradient in the unresolved galaxy light. Thus, in order to properly background-subtract the tip-tilt wavefront sensor, the sky background was measured at a manually selected sky position such that the light

Night	No. of frames	Position
2008 Oct 21	13	center
2010 Aug 15	18	center
2010 Aug 28[a]	22	NW, SE
2010 Aug 29	23	NW, SE

Note.
[a] Night removed from analysis owing to poor spatial resolution.

from M31's bulge had comparable intensity to that of the tip-tilt object positions.

2.1.1. Keck/OSIRIS

Spectroscopic measurements of the M31 nucleus were made using OSIRIS (Larkin et al. 2006), an IFU spectrograph, on 2008 October 21 (PI: M. Rich), 2010 August 15 (PI: J. Lu), and 2010 August 28–29 (PI: A. Ghez; Table 1). The individual OSIRIS data cubes cover $0\rlap{.}''8 \times 3\rlap{.}''2$ and were oriented at a P.A. of $56°$ along the major axis of the eccentric stellar disk. The field was sampled with a pixel scale of $0\rlap{.}''05$ pixel^{-1}, and each spatial pixel (spaxel) provides an independent spectrum across the K-broadband filter (Kbb: $\lambda = 2.18 \mu m$, $\Delta \lambda = 0.4 \mu m$) with an average spectral resolution of $R \sim 3600$. A total of 76 individual exposures were taken with $t_{exp} = 900$ s in a 3×1 mosaic pattern. Observations taken the night of 2010 August 28 were subject to poor weather; the spatial resolution of these frames was generally poor (see Section 3.2), and thus these frames were removed from the analysis, leaving 54 total exposures. Observations on two of the remaining three nights were centered on the field, while the northwest and southeast pointings of the mosaic were observed on the other night. On each night, observations of telluric standard stars and blank sky were also obtained for use in calibration.

Total integration time on the center of the field consists of ~ 35 exposures (9 hr), while the edges of the FOV were observed in 5–20 exposures (1.25–5 hr; see Figure 2, bottom panel).

2.1.2. Keck/NIRC2

New supporting NIR imaging of the M31 nucleus was taken with NIRC2, the facility NIR camera on Keck. On 2005 July 29, a total of eight images were taken in the K'-band filter ($\lambda = 2.12 \mu m$, $\Delta \lambda = 0.35 \mu m$) with 30 s exposure times (PI: K. Matthews).

On 2009 September 10, the nucleus was imaged with NIRC2 using the J-band ($\lambda = 1.25 \mu m$, $\Delta \lambda = 0.16 \mu m$) and H-band ($\lambda = 1.63 \mu m$, $\Delta \lambda = 0.30 \mu m$) filters. Exposure times were 120 and 60 s, respectively. A total of 15 frames were combined for the final J image, and 14 frames were used for the H image (PI: A. Ghez).

The J, H, and K' images described above were all taken using the narrow camera, which provides a pixel scale of $0\rlap{.}''01$ pixel^{-1}. Wide camera images, with a pixel scale of $0\rlap{.}''04$ pixel^{-1}, were obtained from the Keck Observatory Archive from observations taken on 2007 October 19 during engineering time with NIRC2 using the K' filter. One exposure was used, with five co-adds of 1 s integration time each, for a total exposure time of 5 s.
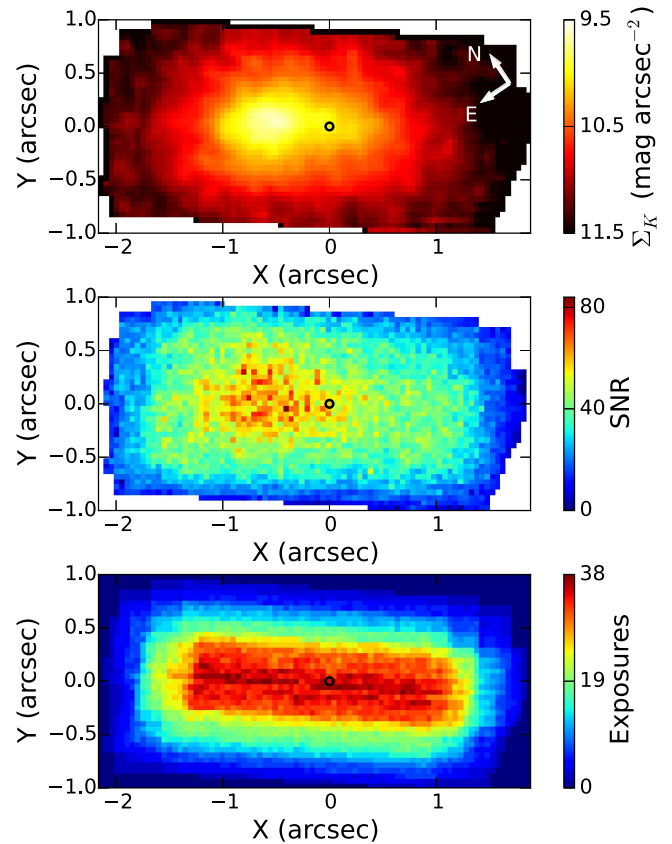
Figure 2. Data quality maps of the OSIRIS mosaic, using data from 2008 October 21, 2010 August 15, and 2010 August 29. Top: mosaic of all OSIRIS frames from these three nights, collapsed along the wavelength direction. Middle: S/N map calculated using a line-free portion of the continuum. Bottom: number of exposures combined at each spaxel in the mosaic.

2.2. HST

Supporting archival imaging of the nucleus from *HST* was also used. Optical images of the M31 nucleus were obtained with *HST* and downloaded from the Hubble Legacy Archive. The nucleus was imaged on 2006 June 15–16 using the Advanced Camera for Surveys (ACS) High Resolution Channel (HRC) with the F330W and F435W filters (PI: T. Lauer; Lauer et al. 2012). Total exposure time with the F330W filter was 8120 s over 12 exposures, while the total exposure time with the F435W filter was 2384 s over eight exposures.

The nucleus was imaged on 1994 October 02 using the Wide Field and Planetary Camera 2 (WFPC2) with the F555W, F814W, and F1042M filters (PI: M. Rich; Rich et al. 1996). Total exposure time for the F555W filter was 1680 s over six exposures, for the F814W filter was 1280 s over five exposures, and for the F1042M filter was 5000 s over 10 exposures.

3. Analysis

3.1. OSIRIS Data Reduction

The OSIRIS spectroscopic data were reduced using the OSIRIS reduction pipeline[7] (Krabbe et al. 2004) to subtract a dark frame, correct bad pixels and cosmic rays, perform the data cube assembly and wavelength calibration, and remove the

---

[7] github.com/Keck-DataReductionPipelines/OsirisDRP

background sky and telluric OH emission. The pipeline version utilized for the reduction was v3.2. The pipeline includes internal logic to account for the hardware changes that have occurred since the data were taken and uses the modules appropriate for the date of observations.

For each data cube, the telluric absorption spectrum was modeled and removed using a combination of empirical and theoretical telluric absorption spectra. The empirical telluric spectrum was created using two standard stars with different spectral types as described in Hanson et al. (1996). A hot, early-type A0V star was observed (HD 209932) each night. This star has a featureless blackbody spectrum in the K band, except for a wide Brγ absorption feature at 2.166 μm. A solar-type star was also observed (HD 218633) each night and divided by a solar spectrum constructed from NSO data by ESO and convolved to match the OSIRIS spectral resolution (Livingston & Wallace 1991; Maiolino et al. 1996) to obtain a telluric spectrum. The solar-type telluric standard was used to replace the region around Brγ, from 2.151 to 2.181 μm, in the A0V spectrum. The corrected A0V spectrum was then divided by a 9500 K blackbody to obtain the final empirical telluric absorption spectrum.

However, changing atmospheric conditions throughout each night and a variable spectral resolution across the OSIRIS FOV led to large residuals when correcting for telluric absorption using the empirical telluric spectrum, which was observed at only a single detector location. This was specifically an issue where blueshifted stellar CO bandheads in the M31 spectra overlap with the large telluric residuals. To better model the changing telluric line depths, we created model telluric spectra with the molecfit package (Kausch et al. 2015; Smette et al. 2015), which generates synthetic telluric absorption spectra. Given an atmospheric profile for a given night and observatory location, molecfit uses a radiative transfer code to obtain absorption line depths and fits the output directly to the telluric features in a science spectrum. Before using molecfit, the OSIRIS M31 science frames were first mosaicked by night and by pointing, roughly corresponding with first and second half-nights, to better capture temporal telluric variations. A subset of 3×3 spaxels was extracted from a region of each mosaic where the stellar absorption lines did not overlap with the telluric lines. The median of these spectra was taken to create a single typical spectrum per half-night, and molecfit was run on each of these representative spectra to obtain the telluric absorption line depths. However, these model spectra could not be used directly in the telluric correction, as OSIRIS introduces a shape to the continuum that is not fit well by the molecfit modeling. The resulting molecfit line depths were combined with the continuum from the empirical telluric spectrum to produce a final telluric absorption spectrum, which was used to telluric-correct the M31 data.

The final mosaic was assembled by calculating shifts between frames using cross-correlations between each OSIRIS frame and the NIRC2 K-band image, rebinned to the OSIRIS spatial scale. Frames within a single dithered set (typically four to nine frames) were first mosaicked together, as the offsets between these frames are given by the input dithers. Each of these mosaics was then cross-correlated with the NIRC2 image to obtain its relative shift. The frames were then combined using a mean clipping method. The final OSIRIS data set consists of one fully combined data cube and three subset

cubes, each containing 1/3 of the data, used for determining uncertainties.

### 3.2. Flux Errors and Data Quality

The formal errors output by the pipeline include real spatial and spectral variations caused by removed OH sky lines, telluric absorption, interpixel sensitivity, and cosmic rays. However, the overall error is too large by nearly an order of magnitude relative to empirical error estimates, determined via the standard error on the mean of three subset cubes at each spaxel and spectral channel. As the magnitude of the flux errors impacts the errors on the kinematic measurements (Section 3.6), the errors need to be properly scaled. To combine the error variation captured by the formal pipeline errors with the more accurate magnitude of the empirical errors, we scale the pipeline errors by the ratio of the median of the two error arrays at every spaxel. We adopt these scaled flux errors for the remainder of the analysis.

The OSIRIS image quality was estimated by first collapsing the cube along the spectral direction. Then the OSIRIS image was compared to the NIRC2 image by convolving the NIRC2 image with an iteratively determined kernel that reduced the difference between the NIRC2 and OSIRIS images. A Gaussian kernel was used to represent the diffraction-limited core. The amplitude was set to 1 and not allowed to vary, while the width of the core Gaussian was allowed to vary. This gives an estimate of the spatial resolution of the OSIRIS images compared to the NIRC2 images. The resulting spatial resolution ranges between 50 and 350 mas FWHM for the individual exposures, and the median spatial resolution across all frames is 260 mas. The majority of the lower-quality frames are in the southeast pointing of the mosaic, due to worse observing conditions during the nights this pointing was observed. We experimented with removing various combinations of the lowest-quality frames, striving to maintain even coverage across the FOV. Ultimately, all frames from 2010 August 28, the night with the worst weather, were removed, resulting in a median spatial resolution of 205 mas among the remaining frames and a resolution of 124 ± 6 mas for the full combined mosaic (Figure 3). We proceeded with the analysis using this clipped set.

3.3. Bulge Subtraction

The old stellar population of the bulge is the dominant source of light at $5\farcs5 < r < 300''$ (Kormendy & Bender 1999, hereafter KB99) and is a source of foreground contamination in observations of the nuclear disk. In addition to being a source of excess surface brightness, the bulge's slow rotation and internal dispersion can distort the kinematic signature of the nuclear disk. Both the surface brightness and the kinematic contribution of the bulge must be removed before extracting the nuclear disk kinematics.
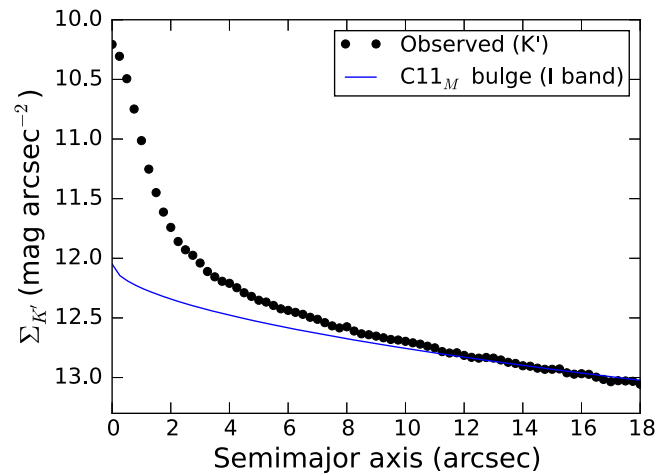
First, we determined the fraction of bulge light in each spaxel. Previous studies have found that both the optical and the NIR surface brightness profile of the bulge is well fit by a Sérsic profile (KB99; Courteau et al. 2011; Dorman et al. 2013) of index $\sim$2, half-light radius $\sim$1 kpc, and half-light surface brightness 17.55–17.85 mag arcsec^{-2} (optical V band, $\lambda = 555$ Å, and I band, $\lambda = 806$ Å) or 15.77 mag arcsec^{-2} (L band, $\lambda = 3.6$ μm). The I-band surface brightness profile from Courteau et al. (2011, model M) was adopted and scaled
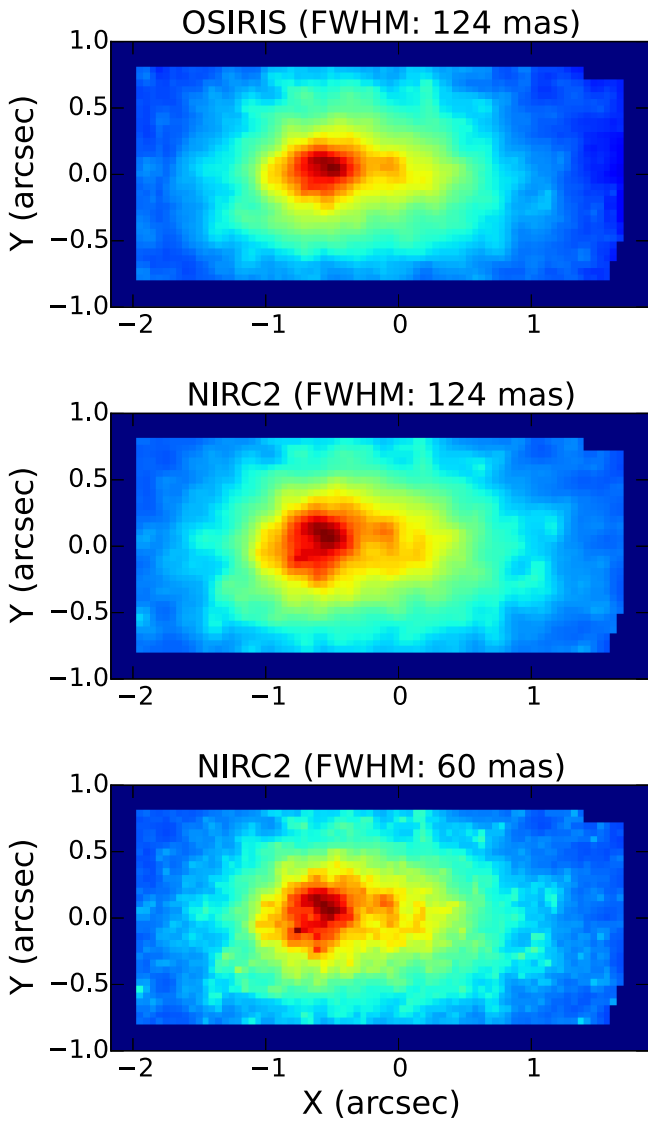
Figure 3. The spatial resolution of the combined OSIRIS mosaic was determined by comparing it with a high-resolution K-band NIRC2 image convolved with a Gaussian. Top: OSIRIS data cube, collapsed in the wavelength direction. Middle: NIRC2 K-band image, convolved to the same spatial resolution as the OSIRIS cube. Bottom: original NIRC2 image, binned to the same pixel scale as the OSIRIS data.

Figure 4. Profiles for the bulge surface brightness (Courteau et al. 2011) match measured K-band surface brightness profiles well beyond 11″. The flux-calibrated K-band surface brightness profile is measured from the NIRC2 wide camera image and is calculated in elliptical apertures using the ellipticity given by Courteau et al. (2011). The bulge profile is given in Courteau et al. (2011, their model M); an additive offset has been applied to the bulge profile so it matches the flux level in the K band at 15″, necessary because of the flux difference between the two bandpasses.
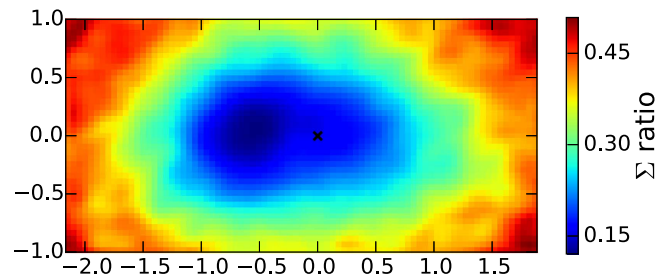
Figure 5. Ratio of the bulge luminosity to the total K-band luminosity within the nuclear region, derived using the I-band Sérsic profile (model M) from Courteau et al. (2011) in comparison with the NIRC2 K-band image. The SMBH position is marked with the black cross, and the orientation is as in Figure 2.

to match the NIRC2 K-band wide-field image at a radius of 10″, or a distance at which the bulge dominates the surface brightness (Figure 4). The 1D Sérsic profile was converted to a 2D profile using the model M bulge ellipticity. We used the bulge P.A. of 6°.6 from Dorman et al. (2013), as they fit the bulge profile with the same data set; the differences with their best-fit parameters are negligible. Both the 2D bulge profile and the NIRC2 image were smoothed to match the OSIRIS resolution, and the two smoothed images were divided to obtain the ratio of bulge luminosity to total luminosity in the nucleus (Figure 5).

Bulge-dominated spaxels were selected based on the bulge surface brightness ratio map. As no spaxels had a majority contribution from the bulge (Figure 5), those spaxels in which the bulge surface brightness ratio is at least 0.42 were selected to be representative of the bulge. This ensures that enough spaxels, roughly 160, were obtained to derive a high-quality bulge template spectrum.

Next, the intrinsic spectrum of the integrated bulge light was estimated using the penalized pixel fitting (pPXF) package (Cappellari & Emsellem 2004), which fits a linear combination of stellar templates convolved with a line-of-sight velocity distribution (LOSVD). pPXF was also configured to fit and add a fourth-degree Legendre polynomial to the convolved spectrum, to account for continuum shape differences between the stellar templates and the science spectrum (see Section 3.6 for more details). The bulge-dominated spaxels were fit with pPXF. The output best-fit linearly combined stellar templates for each spaxel, along with the additive Legendre polynomial, were used to create a template stellar spectrum for each bulge-dominated spaxel. Each resulting template spectrum reflected the flux level of the corresponding spaxel in the data cube. To normalize these spectra, the template spectrum for each spaxel was divided by its median. The median of all normalized bulge template spectra at each wavelength was then taken to obtain a median stellar template for the bulge.

The median bulge spectrum was dominated by two stellar template spectra: a late K giant and a late K dwarf. The late K giant is likely more representative of the actual bulge population, which is estimated to be roughly the age of the galaxy (Saglia et al. 2010). However, the late K dwarf star has stronger Na lines
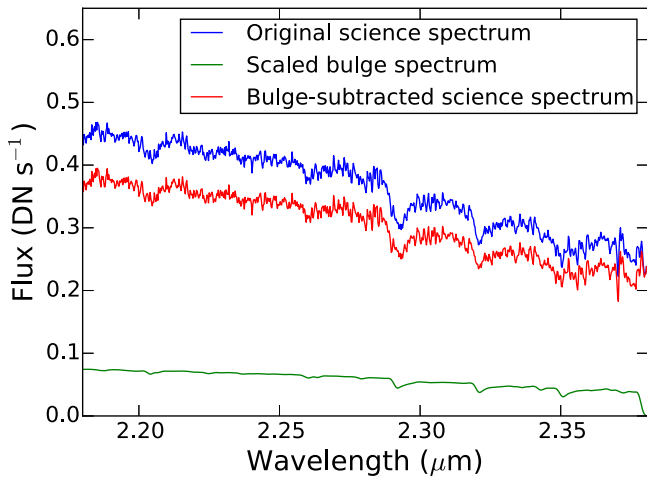
Figure 6. Example science spaxel, before and after bulge subtraction. The spaxel is taken from near the center of the cube and is shown before and after bulge subtraction. The bulge spectrum, convolved with the bulge LOSVD and scaled per the ratio given in Figure 5 for the example spaxel, is also shown.

Table 2
SMBH Alignment

Telescope	Instrument	Filter	$N_{sources}$[a]	Error[b] (arcsec)
HST	ACS	F330W	…	…
HST	ACS	F435W	16	0.0093
HST	WFPC2	F555W	26	0.013
HST	WFPC2	F814W	16	0.018
HST	WFPC2	F1042M	19	0.016
Keck	NIRC2	*J* band	19	0.015
Keck	NIRC2	*H* band	18	0.0065
Keck	NIRC2	K' band	18	0.0063

Notes.
[a] Number of sources used to align the given frame with the next bluer frame.
[b] Alignment error in the SMBH position from each coordinate transformation.

than that of the giant. The center of M31 is estimated to have enhanced metallicity compared to the Milky Way (Saglia et al. 2010), and thus the inclusion of the dwarf stellar template in the fit may be compensating for this different abundance pattern. Alternatively, varying Na line strengths may represent variation in the initial mass function of the old stellar population (McConnell et al. 2015, and references therein).

Finally, the bulge spectrum was convolved with a Gaussian LOSVD with a fixed velocity of $-340\,\mathrm{km\,s^{-1}}$, at the systemic velocity of the galaxy (R. Bender 2018, private communication), and a dispersion of $110\,\mathrm{km\,s^{-1}}$ at all points in the field, or the dispersion in the bulge-dominated spaxels before bulge subtraction. No bulge rotation was included since previous work by KB99 found that the bulge is rotating slowly at $2.65(r/1'')\,\mathrm{km\,s^{-1}}$ and that including this rotation does not appreciably affect the bulge subtraction within the compact nuclear region. The final bulge spectrum was multiplied by the median flux in each spaxel and the appropriate surface brightness ratio to create a bulge cube. This cube was then subtracted from the observed spectral cube. An example spectrum, before and after bulge subtraction, and the scaled bulge template spectrum are shown in Figure 6.

There are systematic sources of error in the bulge subtraction that we do not fully explore but that should be kept in mind. The edges of the OSIRIS FOV are subject to much more bulge subtraction than the center (Figure 5). Subtracting so much flux ends up amplifying the noisiness of the bulge-subtracted spectrum. This noise is not purely Poissonian, but also includes noise from imperfectly corrected sky and telluric features, which introduce larger systematic errors into the spectra at the edge of the FOV. In addition, the bulge is typically modeled as a Sérsic profile, which is sharply peaked at the origin. However, Bacon et al. (2001) also fit the bulge using a multi-Gaussian expansion (MGE), which models the bulge surface brightness as the sum of three Gaussians. Their MGE bulge profile is much shallower in the inner few arcseconds, with a difference of a few tenths of a magnitude at the origin from the equivalent Sérsic profile. Alternative bulge subtraction methods may subtract more or less flux than does our method, which may impact the kinematics derived from the bulge-subtracted spectra. In Appendix A, we explore in more detail several alternative methods of bulge

subtraction and show that their impact does not change the overall conclusions of this paper.

3.4. Position of the SMBH

We identified the position of the SMBH in our OSIRIS and NIRC2 data using the position of P3, the very compact ($r \sim 0''.06$; Lauer et al. 1998) young nuclear cluster that contains the SMBH (Bender et al. 2005). Unlike the old stellar population, which is bright in the NIR, P3 is NIR-dark and thus effectively invisible in our OSIRIS and NIRC2 data. However, P3 is bright in the UV; we adopted as the SMBH position the location of source 11, or the brightest UV source in the Lauer et al. (2012) analysis of *HST*/ACS F330W and F435W images. The NIR image cannot be directly aligned to the F330W image because there are no compact sources that are bright in both the blue and NIR filters that can be used to determine the transformation. Instead, we aligned images at successively longer wavelengths using an evolving set of compact, bright sources to fit the translation, scale, and rotation (Table 2), aligning adjacent-bandpass frames using only the sources common to both frames (see Appendix B). At least 16 bright compact sources are used for aligning each pair of frames. After alignment, each frame was transformed into the reference frame, F330W. The error on each frame's alignment was taken as the residual error, converted to arcseconds. The total error in alignment from F330W to the NIRC2 *K*-band image is $0''.033$, which is smaller than the $0''.05$ spaxels in the OSIRIS data. The OSIRIS data cube was aligned to the NIRC2 *K*-band image by cross-correlating the OSIRIS cube, collapsed in the wavelength direction, with the final registered NIRC2 *K*-band image.

Figure 7 shows the region within $0''.3$ of P3 in each of the eight wavelength images after alignment. The pixel scaling was adjusted in each frame to match that of the F330W image. The SMBH coordinates were taken from the background-subtracted, subsampled F435W image (Lauer et al. 2012, private communication) and converted to the aligned K'-band image coordinates. The SMBH position is marked with the black cross in each panel in Figure 7.

3.5. Spatial Binning

Fitting the precession rate of the disk requires a very high signal-to-noise ratio (S/N). The S/N of the data varies over the FOV and was calculated empirically. For each spaxel, we fit a straight line in a region of the spectrum dominated by the stellar continuum between 2.270 and 2.280 μm. After dividing by the
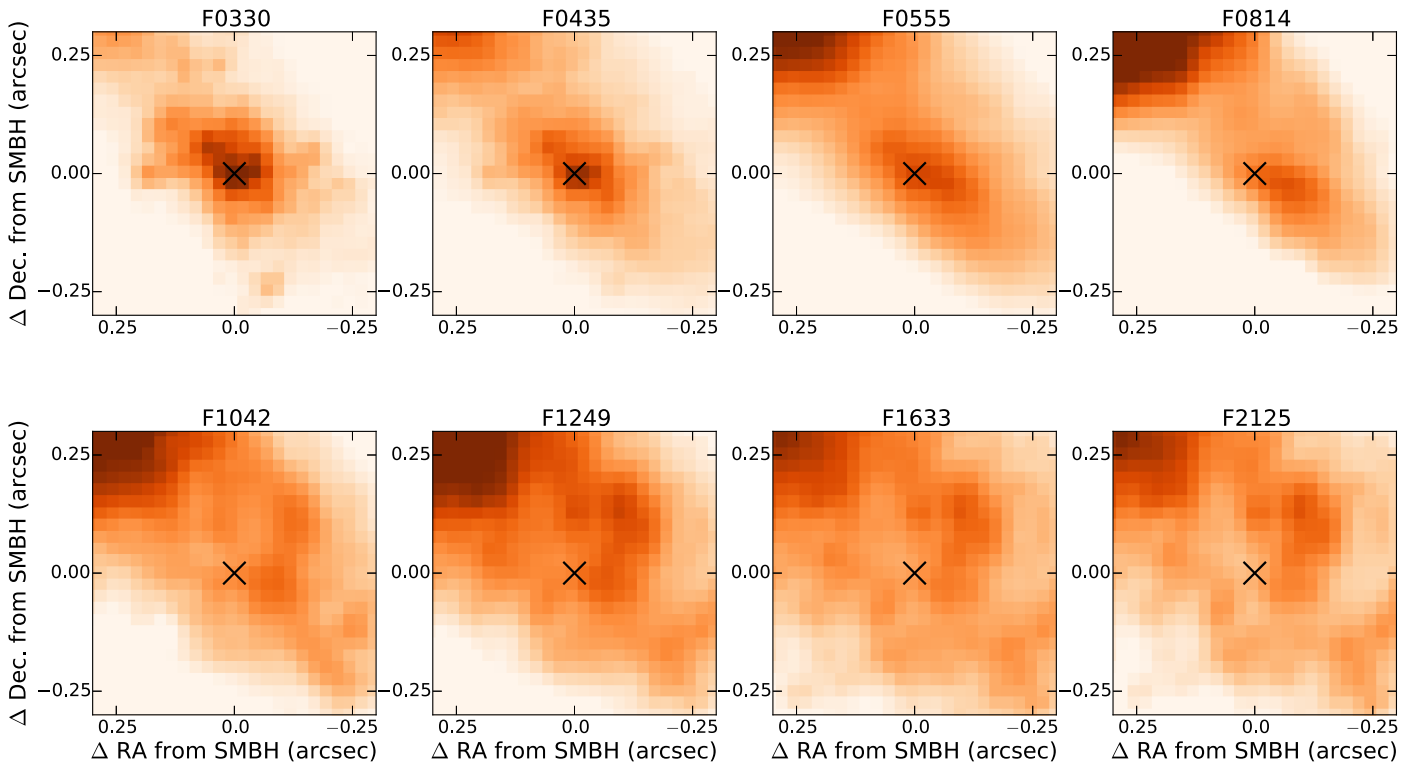
Figure 7. Multiwavelength images show the changing stellar population from 330 nm (F0330) to 2.1 μm (K'). The position of P3, assumed to be coincident with the SMBH, is marked with the black cross and is accurate to $0''033$ in the K'-band frame. The color scaling has been adjusted for each frame to emphasize the structure around the SMBH. North is up and east is left, and the pixel scale is $0''025$ pixel^{-1}.

fitted line, the S/N was estimated as the mean of the normalized flux divided by the standard deviation. The S/N map is shown in the middle panel of Figure 2.

The data were spatially binned using a Voronoi tessellation algorithm (Cappellari & Copin 2003), which optimally sums spaxels until a target S/N is reached while enforcing a roundness criterion on the resulting bins to ensure that the resulting bins are as compact as possible. Spaxels already at or above the target S/N remain unbinned. We used the S/N map thus generated to spatially bin the spaxels to a target S/N of 40. The resulting bins and their S/N are shown in Figure 8. Spaxels near P1, P2, and the SMBH remained unbinned, while the fainter outer regions of the eccentric disk and the innermost bulge were optimally binned. Spectra in the binned spaxels were summed and their errors combined in quadrature. Spaxels with a very low initial S/N (<2) on the very edge were masked and discarded in the following analysis.

3.6. Kinematic Fitting

Kinematics were extracted using the pPXF method described in Cappellari & Emsellem (2004). This method fits the observed spectrum with a linear combination of spectral templates, convolved by an LOSVD, which we parameterized as a fourth-order Gauss–Hermite expansion of a Gaussian profile (Appendix A of van der Marel & Franx 1993). A fourth-degree Legendre polynomial was fit and added to the convolved spectrum to correct for mismatch between the continuum of the template and that of the science spectrum. The moments of the best-fit LOSVD (including v, σ, and the higher-order moments h_3 and h_4) and the weights of the spectral templates were returned. The Gemini GNIRS spectral template library (Winge et al. 2009), a library of evolved and main-sequence late-type
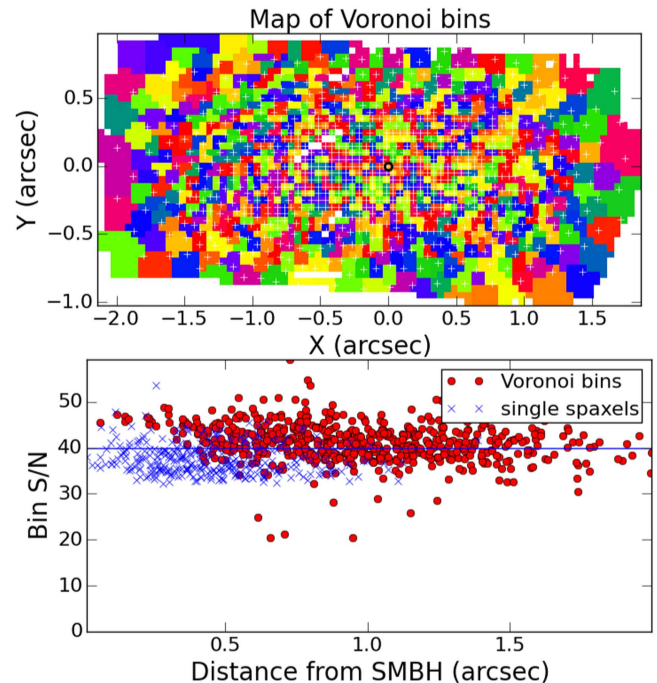
Figure 8. Top: spatial bins determined via Voronoi tessellation (Cappellari & Copin 2003). Spaxels with an initially high S/N remain unbinned, while spaxels with a lower initial S/N are binned until their final combined S/N is roughly 40. The colors are randomized to emphasize bin boundaries. Bottom: final S/N for each bin as a function of distance from the SMBH.

stars observed in the K' band at $R \sim 5900$, was used as inputs to pPXF. Only those templates observed in both the blue (2.15–2.33 μm) and the red (2.24–2.43 μm) modes were used,
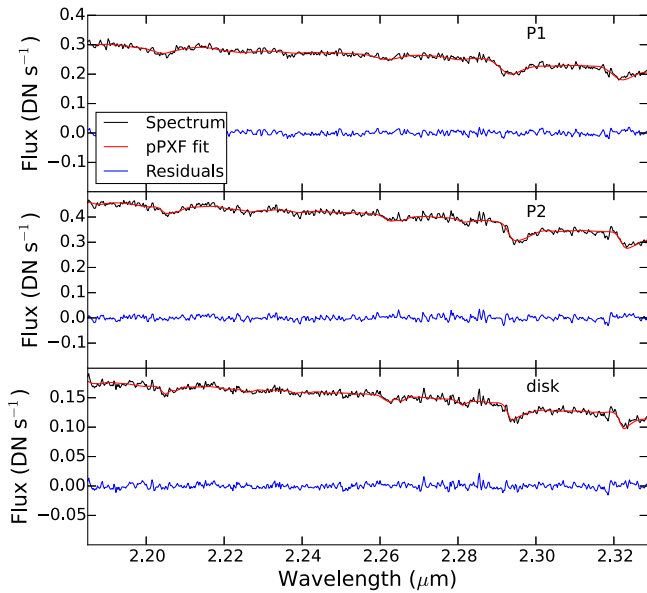
Figure 9. pPXF fits and residuals for three sample spectra. In all, the input science spectrum is shown in black, the best-fit pPXF fit is shown in red, and the residuals between the two are shown in blue. Top: sample spaxel from near the P1 flux peak. Middle: sample spaxel from the P2 region. Bottom: sample spaxel from outside either of these regions, near the zero-velocity line.

for a total of 23 template stars. The final template library covers G4–G5 II, F7–M0 III, K0 IV, and G3–K8 V stars. Independent fits were performed for each spaxel over the range 2.185–2.381 μm to obtain measurements of v, σ, h_3, and h_4. Example fits for spaxels near P1, in P2, and in the disk away from these regions are shown in Figure 9.

The templates preferred by the pPXF fits on the bulge-subtracted stellar population are nearly identical to those found in the fits to the bulge-dominated spaxels. Similar to the bulge population, the old eccentric disk is best fit by a late K giant and a late K dwarf template spectrum. This implies, as found by previous work (Saglia et al. 2010), that the old eccentric disk has a similar stellar population to that of the bulge. However, we defer a full analysis of the eccentric disk stellar population to future work.

Measurement errors on the LOSVD moments were assessed via a Monte Carlo (MC) analysis using 100 simulations. In each simulation, the input spectrum was randomly perturbed within the 1σ flux errors and the pPXF fits were recalculated. The uncertainty of each LOSVD moment (i.e., mean v, σ, $h3$, $h4$) was taken as the standard error of the mean of the fitted moments from the MC trials. Error maps are shown in Figure 10. The median errors are $11.3\,\mathrm{km\,s^{-1}}$ on v and $16.7\,\mathrm{km\,s^{-1}}$ on σ.

In addition to measurement errors, mismatch between the spectral templates and the intrinsic stellar population can provide a source of systematic error. The magnitude of this error was assessed via a jackknife analysis. One spectral template at a time was dropped from the library used in the fitting routine. pPXF fits were run for each of these 23 template library subsets, and the systematic errors from template mismatches were calculated as the standard error of the mean of the resulting outputs. Error maps are shown in Figure 11, and the median errors are $1.3\,\mathrm{km\,s^{-1}}$ on v and $1.6\,\mathrm{km\,s^{-1}}$ on σ. These errors are nearly an order of magnitude lower than the measurement errors and thus negligible compared to the observational error. We disregard this source of error in the remainder of the analysis.

4. Results

4.1. Kinematics of the Eccentric Disk

The results of the pPXF kinematic fitting are shown in Figures 12 and 13. The velocity map shows a clear rotation signature, but with a slight asymmetry in the morphology of the velocity peaks. In addition, the peak of the velocity is offset from the P1 peak flux (Figure 14). There is also an asymmetry in the magnitude of the velocities on either side of the disk, with maxima of $223 \pm 7\,\mathrm{km\,s^{-1}}$ on the northeast side and $-312 \pm 16\,\mathrm{km\,s^{-1}}$ on the southwest side. In addition, the zero of the velocity gradient does not coincide with the SMBH position, but is offset by $0\rlap{.}''15$ toward P1, which is consistent with previous long-slit measurements (Bender et al. 2005).

The dispersion is peaked close to but not at the position of the SMBH as is shown in the zoomed kinematic maps in Figure 13 and in the contour plot in Figure 14. The dispersion reaches a maximum of $381 \pm 55\,\mathrm{km\,s^{-1}}$ at an offset in (x, y) of $(+0\rlap{.}''09, -0\rlap{.}''1)$ from the SMBH, or a distance of $0\rlap{.}''13$ on the P2 side. The wider dispersion peak ($\sigma > 200\,\mathrm{km\,s^{-1}}$) is concentrated on the P2 side and extends toward P1.

Overall, the maps for the higher-order moments $h3$ and $h4$ are quite noisy, and trends are difficult to discern. There is a possible enhancement of $h4$ on the P1 side of the SMBH, but the results are not robust. We find that the significance of the $h3$ and $h4$ maps is particularly sensitive to the bulge subtraction.

4.2. Comparison to Previous Multiwavelength Imaging

Closer examination of Figure 7 shows that there are clear differences in the structure of the stellar population at each wavelength; notably, P3 is bright and compact only in the F330W and F435W frames and is dark in the NIR. Figure 15 shows the inner $0\rlap{.}''2$ in the F330W, background-subtracted F435W (Lauer et al. 2012, private communication) and K' images, with the SMBH position marked. In contrast with the bluer images, there is little to no flux at the position of P3 and the SMBH in the NIR, indicating a separation of the young and old stellar populations in the nucleus.

A clearer comparison of the difference between the flux maps at two different wavelengths can be seen in Figure 16. Lauer et al. (1998) observed the nuclear eccentric disk with *HST*/WFPC2 in three filters: F300W, F555W, and F814W. We show their F555W flux map, convolved to the OSIRIS spatial resolution, in comparison with the OSIRIS flux map. There are clear structural differences visible between the two flux maps, particularly around the P1 peak. In addition, the morphology differences seen around the SMBH in Figure 7 can been seen here: the secondary P2 peak is more northerly in the OSIRIS data than in the F555W image.

This structural difference can also be seen in 1D cuts across each image (Figure 17). A 1D cut has been taken across each frame in Figure 7 at the P.A. of the *HST*/STIS long-slit observations (see Section 4.3) and passing through the SMBH. Each 1D cut has been flux-calibrated according to the published instrumental zero-points. The nucleus is much brighter in the NIR than at UV or optical wavelengths, so offsets in magnitudes (shown in the figure legend) have been added to each cut to equalize them on the P1 side. The UV peak at the origin in the F330W and F435W frames is apparent. The optical bandpasses show an extended, shallower flux peak roughly coincident with the SMBH position and extending slightly to the southwest. However, the H and K' flux cuts do
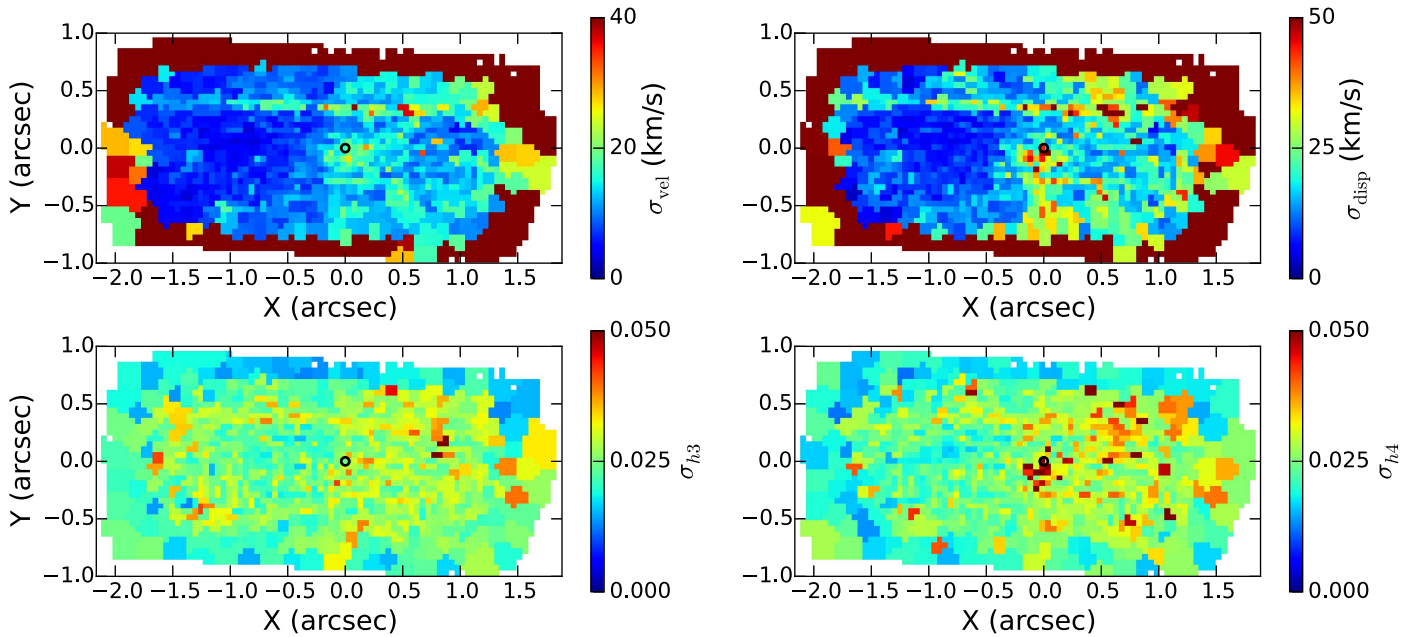
Figure 10. Monte Carlo error maps for the velocity (top left), dispersion (top right), $h3$ (bottom left), and $h4$ (bottom right). In all panels, the SMBH position is marked by the black circle.
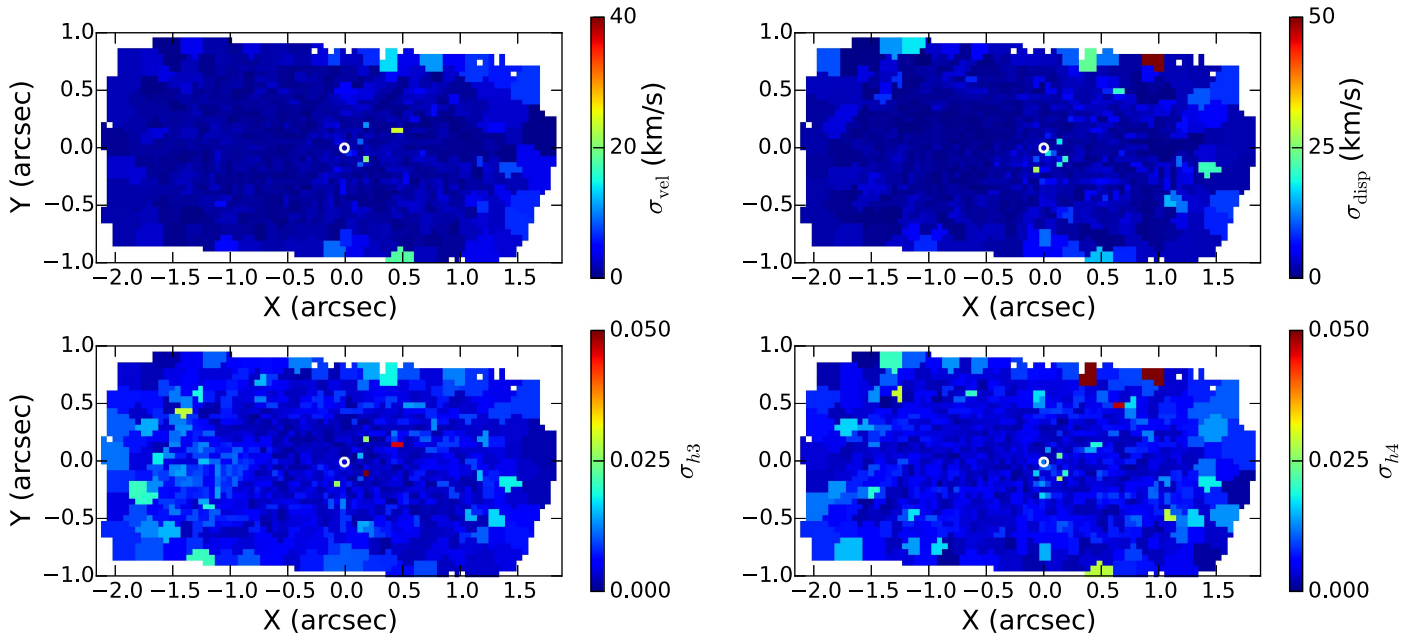
Figure 11. Jackknife error maps, to test for template mismatch to the data for the velocity (top left), dispersion (top right), $h3$ (bottom left), and $h4$ (bottom right). In all panels, the SMBH position is marked by the white circle.

not show this shallower peak and instead are flat from the SMBH position to the cutoff at the southwest edge.

4.3. Comparison to Previous Spectroscopy

The nucleus of M31 has been well studied with both ground- and space-based spectroscopic observations. Several recent studies are summarized in Table 3. In this section, we compare the OSIRIS kinematics with two high-resolution data sets: *HST*/STIS long-slit observations reported in Bender et al. (2005, hereafter B05), and ground-based IFS observations reported in Bacon et al. (2001, hereafter B01).

4.3.1. Comparison with STIS

HST/STIS long-slit spectroscopy was obtained for the nucleus of M31 in 1999 July; the full analysis was published in B05. Spectra were taken in both blue (2900–5700 Å) and red (8272–8845 Å, the Ca triplet) modes; we confine our discussion solely to the red mode. The slit was oriented at a P.A. of 39°, along the major axis of the optical disk. The slit width was 0″1, and the estimated resolution is FWHM = 0″12.

We compare the kinematics reported in B05 with our OSIRIS kinematics in Figure 18. In addition to the original STIS kinematics, we show the STIS kinematics smoothed along the slit by a Gaussian kernel derived using the OSIRIS
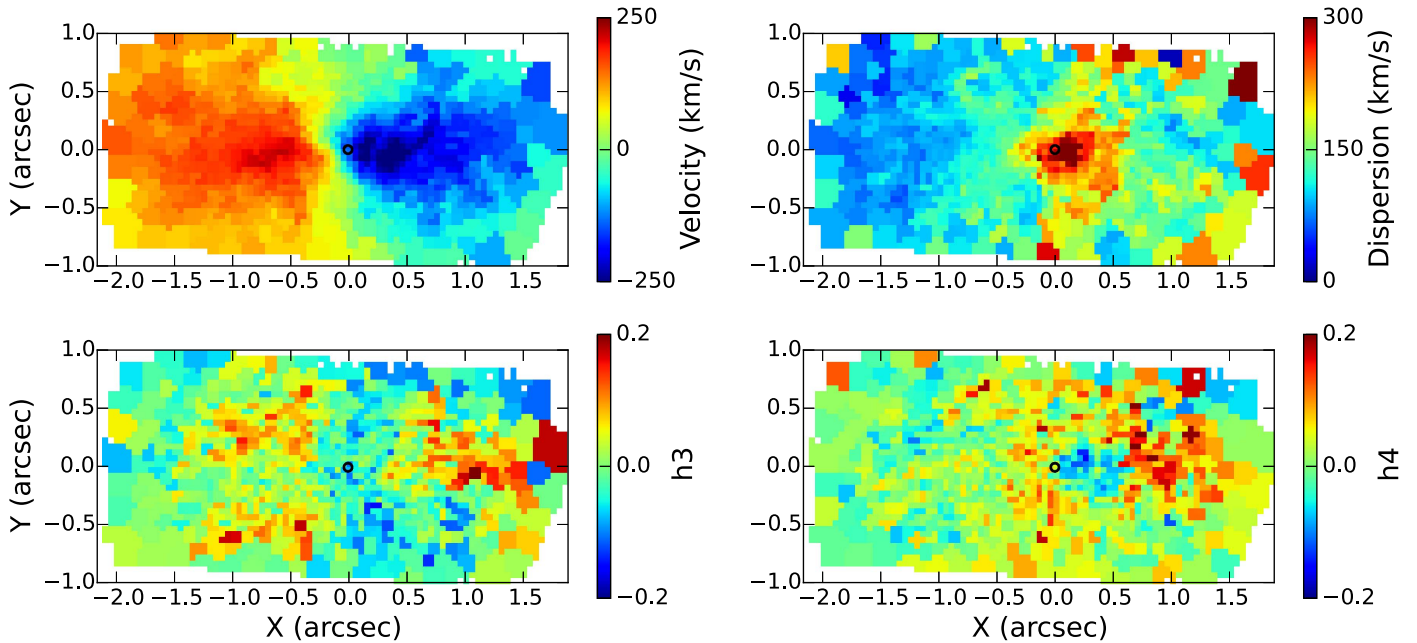
Figure 12. Kinematic maps, as calculated with pPXF (see text). In all panels, the SMBH position is marked by the black circle. Top left: velocity map, shifted by the systemic velocity. Top right: velocity dispersion. Bottom left: *h3*, or the first asymmetric higher-order moment of the LOSVD. Bottom right: *h4*, or the first symmetric higher-order moment of the LOSVD.
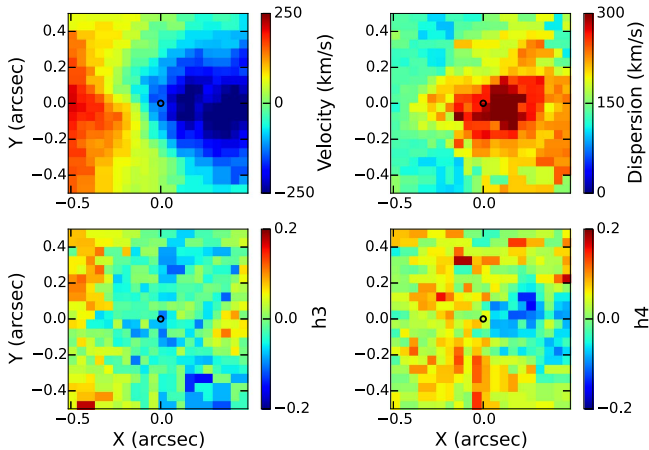
Figure 13. Kinematic maps from Figure 12, zoomed in to the central arcsec around the SMBH (black circle). Top left: velocity map, shifted by the systemic velocity. Top right: velocity dispersion. Bottom left: *h3*. Bottom right: *h4*.

Figure 14. Kinematic contours overlaid on the OSIRIS cube, collapsed in the wavelength direction. In both, the contours have been slightly smoothed and the SMBH is marked with a black circle. Top: velocity contours, in steps of 100 km s^{-1}, with the lowest contour at -200 km s^{-1} shown in dark blue. Bottom: dispersion contours, in steps of 100 km s^{-1}, with the lowest contour at 200 km s^{-1} shown in dark blue.

point-spread function (PSF). The comparison to the OSIRIS kinematics was derived by taking a cut across the kinematic maps in Figure 12 at the STIS P.A. Each point along the STIS slit is represented by the mean of three OSIRIS spaxels orthogonal to the slit to match the STIS slit width, and the errors are taken as the Monte Carlo errors of the same spaxels, added in quadrature.

Though overall the kinematics reported by STIS and by OSIRIS are similar, there are several inconsistencies, particularly in the velocity and dispersion. Overall, while the velocity gradient from the OSIRIS data is well matched to that from STIS, the OSIRIS data show lower peak velocities on both the red- and blueshifted sides of the nuclear disk than the STIS kinematics. In addition, the wings of the velocity profile from OSIRIS are lower than those from STIS, which may point to residuals arising from differences in the bulge subtraction

methods. The peak dispersion values are the same, within the errors, but the OSIRIS dispersion peak is broader, with a possibility of a secondary dispersion peak at 0″.5, on the P2 side. This extended enhanced dispersion in the NIR-bright old stellar population could be probing the apoapse of the eccentric disk.
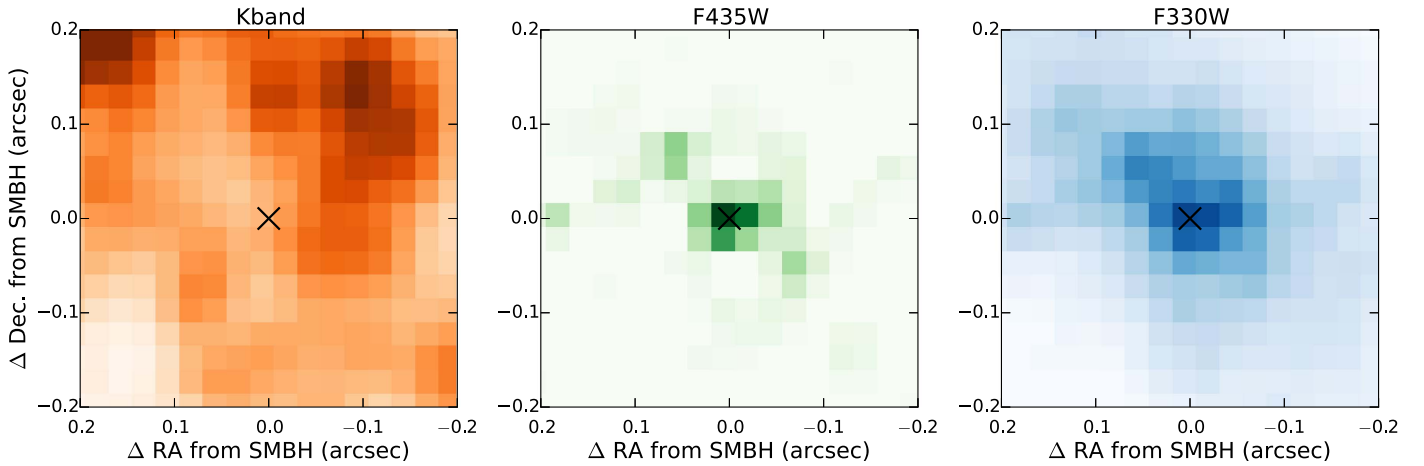
Figure 15. Position of the SMBH, taken as source 11 in *HST*/ACS F435W in Lauer et al. (2012) and calculated in the NIR by aligning with the UV data (see text). The SMBH is shown as the black cross in each panel. Note that P3, coincident with the SMBH and bright in the bluer bandpasses, is not seen above the detection limit in the *K*-band image. Left: NIRC2 *K*-band image; middle: background-subtracted F435W image (T. R. Lauer 2018, private communication); right: F330W image. All frames have been aligned and scaled to the F330W image (0.″025 pixel⁻¹).

4.3.2. Comparison with OASIS

AO-corrected integral field spectroscopy was obtained by the OASIS instrument on CFHT and first presented in B01. Two different mosaics of different spatial resolution were presented, with resolution ranging from 0.″41 to 0.″5. Similar to the STIS data, the chosen wavelength range was 8351–9147 Å to optimize observations of the Ca triplet. OASIS provides a $4'' \times 3''$ FOV.

We show the bulge-subtracted OASIS kinematics in Figure 19. These kinematics were extracted along the OASIS kinematic major axis (P.A. $= 56°.4$) and were initially presented in B01 (their Figure 10, solid line). We also show a cut across the OSIRIS kinematics at the same P.A. The red points are the original OSIRIS kinematics, and the red curve is the OSIRIS kinematics smoothed to the OASIS resolution. The B01 velocity and dispersion profiles have been shifted by $-0.″1$, to better align the velocity gradient with that of the OSIRIS data and to account for differing SMBH positions. Overall, the OASIS velocity profiles agrees well with the smoothed OSIRIS data and are similar to the correspondence seen between the OASIS and STIS kinematics, as reported in B01 (their Figure 13). However, the OASIS and OSIRIS kinematics are not quite aligned along the radial direction. This offset is potentially due to a difference in SMBH position between the OASIS and OSIRIS data; shifting the comparison cut in the OSIRIS data by up to 0.″1 from our SMBH position brings the data into closer alignment along the radial direction, though the correspondence is still not perfect. Also, smoothing the OSIRIS kinematics to match the OASIS resolution brings the two velocity profiles into agreement, but the reported OASIS dispersion peak is higher than that seen in the smoothed OSIRIS data. The peak dispersion in the smoothed 2D OSIRIS dispersion map is less than 250 km s⁻¹, or significantly lower than that seen by OASIS. It is unclear how the OASIS data are able to probe the dispersion at such high resolution given that beam smearing should lower the peak resolved dispersion. Differences in bulge subtraction may be the culprit, or else the OASIS resolution may be better than reported.

5. Eccentric Disk Models

We compare the OSIRIS data to the flux and kinematic models from Peiris & Tremaine (2003, hereafter PT03). These Keplerian models were originally fit to *HST* photometry and ground-based long-slit data (KB99) to determine the orientation of the eccentric disk with respect to the larger-scale galactic disk. In this work, we add rigid-body rotation to the models and determine the best-fit precession rate and orientation using the OSIRIS data. Details of the model fitting are described in Section 5.1, and results on the disk orientation and precession are presented in Sections 5.2 and 5.3, respectively.

5.1. Model Fitting

The original disk models consisted of $\sim 10^7$ particles in disk-plane coordinates, which were rotated to two different orientations as described in PT03: the *aligned* model, matched to the orientation of the large-scale galactic disk, and the *nonaligned* model, with orientation parameters left free (Table 4, second and third columns). The aligned models were a poor fit to both our data and those of PT03; thus, we drop the aligned models from the discussion and focus on the nonaligned models. Throughout the model fitting, we adopt the best-fit parameters of the PT03 nonaligned model, including a black hole mass of $M_\bullet = 1.02 \times 10^8 \, M_\odot$, and keep the parameters fixed unless otherwise specified. In order to fit the model to the OSIRIS data, the particles from the nonaligned model were first rotated to an orientation of our choosing as specified by three angles: the inclination of the disk with respect to the sky (θ_i), the angle of the ascending node in the sky plane (θ_l), and the angle from the ascending node to the periapse vector (θ_a). A solid-body rotation was also introduced by adding a fixed rotation speed, Ω_P (in units of km s⁻¹ pc⁻¹), to the disk-plane model velocities. A right-handed coordinate system was assumed, so positive precessions are counterclockwise. For a given set of model parameters, the particles were randomly perturbed in their sky-plane positions using a Gaussian kernel that matched the OSIRIS resolution in order to smooth out features at higher resolutions. The particles were then spatially binned using the tessellated pattern used for the data (Section 3.5), and the line-of-sight
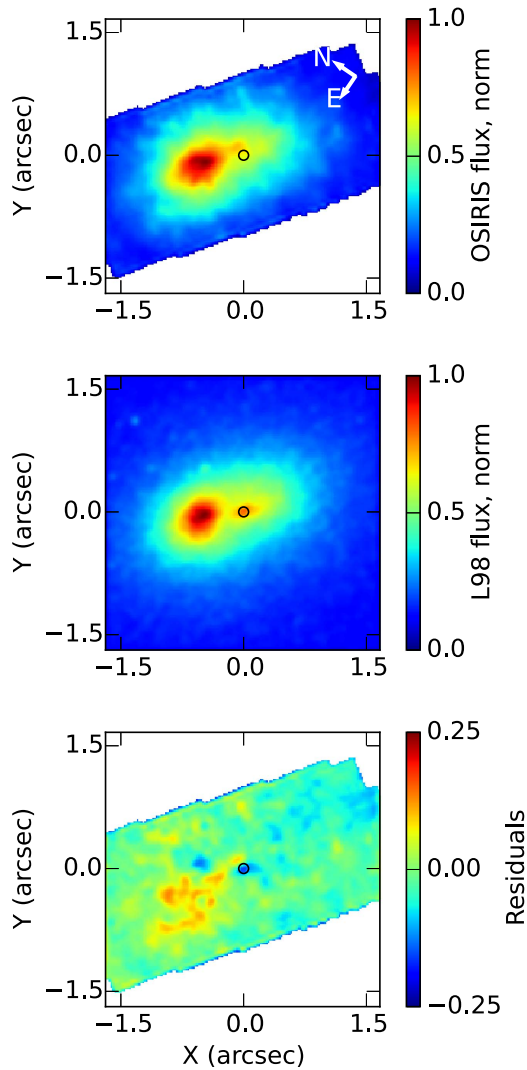
Figure 16. Comparison of OSIRIS flux with that of the F555W flux from Lauer et al. (1998). Top: OSIRIS data cube collapsed in the wavelength direction, rotated to a P.A. of 55°7 and normalized so the peak flux is equal to 1. Middle: F555W flux map from Lauer et al. (1998), normalized so the peak flux is equal to 1, and convolved to match the OSIRIS resolution. Bottom: residuals, taken as the OSIRIS flux minus the F555W flux. In all, the SMBH position is marked with the black circle.

velocities were binned in increments of $5\,\mathrm{km\,s^{-1}}$. The resulting model LOSVD was fit using the Gauss–Hermite expansion in the same manner as the observations.

In order to find the best-fit orientation and precession with our new data, a grid search was performed over Ω_P, θ_i, θ_l, and θ_a. The grid of angles was centered on the original best-fit nonaligned values and spread over a range of $\pm 15°$ with a step of $5°$ for each angle. Precession values in the coarse grid ranged from -30 to $+30\,\mathrm{km\,s^{-1}\,pc^{-1}}$ in steps of $5\,\mathrm{km\,s^{-1}\,pc^{-1}}$.

The goodness of fit was tested by calculating the χ^2, or the sum of the squared residuals between the OSIRIS flux or kinematics and that of the model, weighted by the squared flux or MC errors. Only the flux, velocity, and dispersion moments were used in the fitting process, as the h3 and h4 measurements have lower S/N. For the flux, the OSIRIS data and model were first normalized by dividing by the sum of the flux in each image. Only the inner 1″3 was used for the calculation. The resulting $\tilde{\chi}^2_m$ for each moment, m, was divided by the number
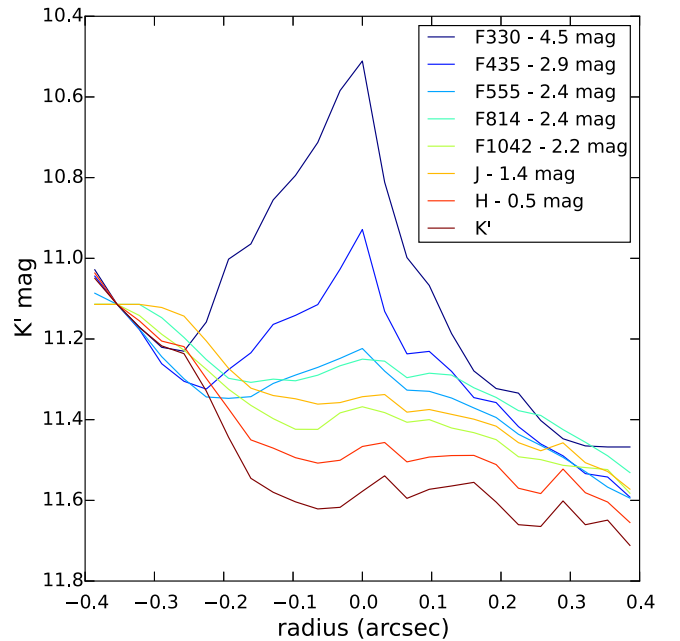
Figure 17. 1D cut across each of the eight wavelength images, at a P.A. of 39° (e.g., the STIS slit P.A.; Section 4.3). Offsets have been added to the cuts in each wavelength, except for the K'-band curve, the brightest wavelength. The offsets were chosen so the flux cuts aligned at roughly the position of P1. The additive magnitude offsets are indicated in the legend.

Table 3
Data Quality Comparison

Instrument	Filter	FWHM	IFU?	Reference
HST FOC	$\sim B$	$\sim 0\rlap{.}''05$	No	Statler et al. (1999)
CFHT SIS	$\sim I$	$0\rlap{.}''63$	No	KB99
CFHT OASIS	$\sim I$	$0\rlap{.}''41–0\rlap{.}''5$	Yes	B01
HST STIS	$\sim I$	$0\rlap{.}''12$	No	B05
Keck OSIRIS	K	$0\rlap{.}''12$	Yes	This work

of spaxels (1746) within the inner region minus the number of free parameters (4), to obtain a reduced $\tilde{\chi}^2_m$. The best-fitting model across all moments was selected based on a weighted sum $\tilde{\chi}^2 = \sum_m \tilde{\chi}^2_m w_m$ over the flux, velocity, and dispersion moments. The weight used was the inverse of the minimum $\tilde{\chi}^2_m$ value for each moment, which is equivalent to error rescaling, in order to prevent any one moment from dominating the fit.

The errors on the best-fit parameters were estimated by performing two Monte Carlo analyses. First, errors were calculated using 100 samples of the data. In each, the flux and kinematic maps were randomly perturbed using a normal distribution matched to the MC errors for the data, and the $\tilde{\chi}^2$ values were recalculated for every model in the grid. Notably, all Monte Carlo samples yielded the same best-fit model parameters as the original, nonperturbed data; however, the best-fit $\tilde{\chi}^2$ for each MC sample varied. To define a 68% (1σ) confidence interval from the data error analysis, we adopted the standard deviation of the best-fit $\tilde{\chi}^2$ values, or $\Delta\tilde{\chi}^2_{\mathrm{data}} = 0.01$. MC errors were also calculated for the models using 100 simulations. In each realization, the model x and y sky-plane position of each particle was perturbed randomly within a Gaussian kernel that matched the OSIRIS resolution. For each MC simulation, the model particles in the best-fit orientation were randomly perturbed within the same Gaussian kernel. To
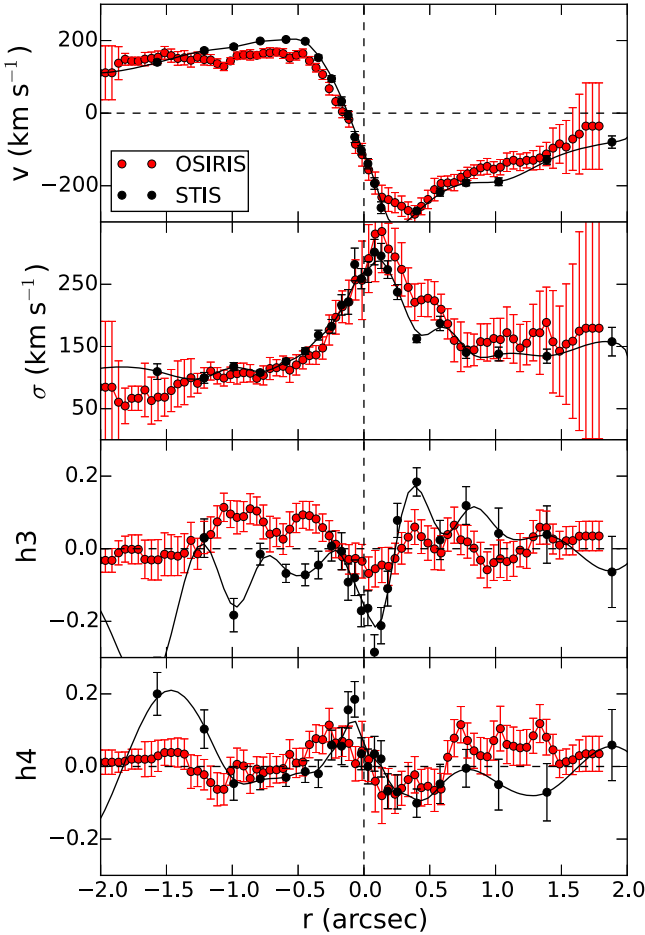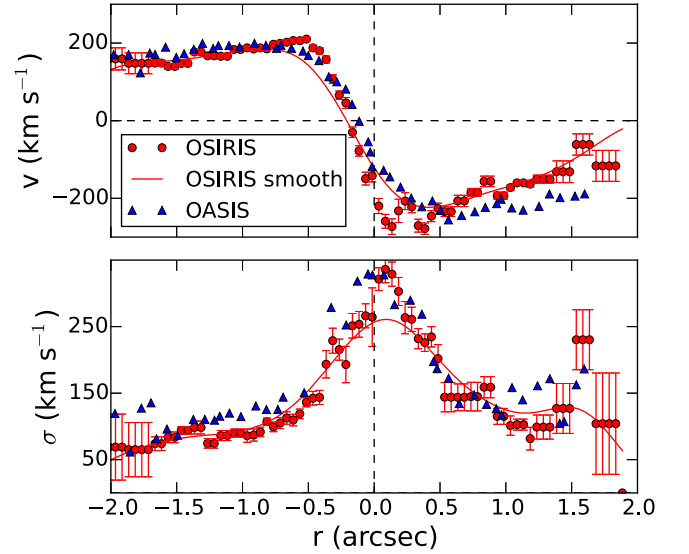
Figure 18. Comparison of OSIRIS and STIS kinematics. The STIS data were taken at a P.A. of 39° and are shown as black points. The STIS data have been smoothed along the slit by the OSIRIS PSF; the smoothed STIS data are shown as the solid black line. A 0″1 width cut, to represent the STIS slit, has been taken across the OSIRIS kinematics at the STIS PA; those data, along with the Monte Carlo errors, are shown in red. All data have been bulge subtracted. The SMBH position is at 0″0, and radius increases toward the southwest.

Figure 19. Comparison of OSIRIS and OASIS kinematics. The OASIS data, shown in blue and taken from their Figure 10, are taken at a P.A. of 56°4, which they identify as their kinematic major axis. The cut across the OSIRIS data, shown in red, is taken at the same P.A., through our SMBH position and parallel to the long axis of the OSIRIS FOV. The red curve shows the OSIRIS kinematics smoothed to the OASIS resolution. All data have been bulge subtracted. Our SMBH position is at 0″0, and radius increases toward the southwest. The OASIS data have been shifted by −0″1 to align the velocity gradients.

Table 4
Model Fitting Results

Parameter	Aligned[a]	Nonaligned[a]	Best Fit[b]
θ_l	−52°3	−42°8	−33° ± 4°
θ_i	77°5	54°1	44° ± 2°
θ_a	−11°0	−34°5	−15° ± 15°
Ω_P [c]	...	...	0.0 ± 3.9

Notes.
[a] PT03.
[b] This work.
[c] Not fit in PT03; units are km s^{-1} pc^{-1}.

define a 68% (1σ) confidence interval from the model stochasticity, we adopted the standard deviation of the $\tilde{\chi}^2$ values from the best-fit models, or $\Delta\tilde{\chi}^2_{model} = 0.08$. The errors from the data and the model MC simulations were added in quadrature, for a total error of $\Delta\tilde{\chi}^2 = 0.08$. Errors on each of the fitted model parameters were derived using this error.

Figure 20 maps the sum of the weighted, reduced $\tilde{\chi}^2$ values for the full range of model parameters that were explored. Figure 21 shows $\tilde{\chi}^2$ values as a function of each parameter in 1D, with the other parameters held constant at their best-fit values. The best-fit $\tilde{\chi}^2_m$ for each moment and the combined $\tilde{\chi}^2$ are shown in Table 5.

5.2. Orientation

Our flux, kinematics, and residuals from the original nonaligned models of PT03 are shown in the left panels of Figures 22–24. We note some discrepancies, particularly in the flux and velocity comparisons. (Following PT03, we note that comparisons between the data and models are only valid within the inner 1″3.) The flux residuals may be due to the difference in morphology of the stellar population at different wavelengths (Section 3.4), as the flux models were originally fit to imaging data taken by *HST* in filter F555W (originally reported

in Lauer et al. 1998) and the kinematics were fit to Ca triplet long-slit data from KB99.

The best-fit models and residuals are shown in the right panels of Figures 22–24. The best-fit orientation is [θ_l, θ_i, θ_a] = [−33° ± 4°, 44° ± 2°, −15° ± 15°]. The 1σ errors are derived using the $\Delta\tilde{\chi}^2$ above. Overall, the fitting preferred smaller values of θ_i and larger values of θ_l and θ_a than those found in PT03 (see Table 6 for a comparison).

5.3. Precession

The reduced $\tilde{\chi}^2$ values for the flux and velocity residuals preferred a positive precession, while the dispersion residuals preferred a negative precession, but overall the preferred precession is $\Omega_P = 0.0 \pm 3.9$ km s^{-1} pc^{-1}. We show the data, model, and residuals for the best-fitting orientation and precession in the right panels of Figures 22–24.

We also fit the precession using the 1D method formulated in Tremaine & Weinberg (1984, hereafter TW84) and modified by Sambhus & Sridhar (2000). Briefly, the original method requires 1D profiles of both the surface brightness and the LOS velocity along the line of nodes, or the intersection of the sky

13
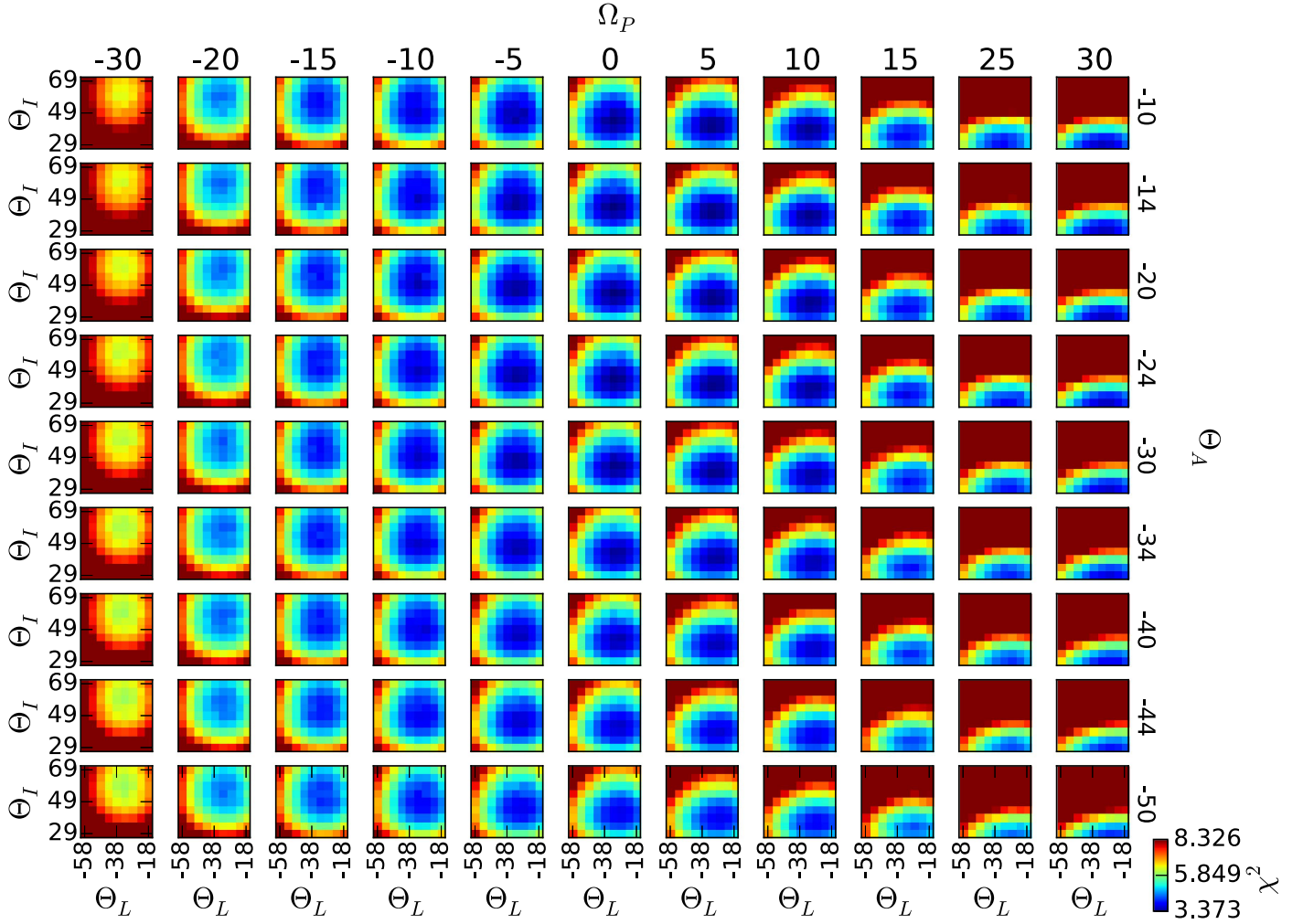
Figure 20. Map of the weighted sum of the reduced $\bar{\chi}^2$ values for the full range of all four modeled parameters (θ_l, θ_i, θ_a, and Ω_P). Each small box shows the range of θ_i (y-axis) and θ_l (x-axis), while θ_a increases along the large-scale y-axis and Ω_P increases along the large-scale x-axis. The color stretch in each panel has been adjusted to emphasize the $\bar{\chi}^2$ minimum.

and disk planes. The modified method allows for the profiles to be taken along the P1−P2 line. In either, the formulation is

$$\Omega_P \sin \theta_i \int_{-\infty}^{\infty} r \, \Sigma(r) \, dr = \int_{-\infty}^{\infty} v_{\mathrm{LOS}}(r) \, \Sigma(r) \, dr,$$

where r is the projected distance from the black hole, $\Sigma(r)$ is the surface brightness, and $v_{\mathrm{LOS}}(r)$ is the line-of-sight velocity.

We take the surface brightness and LOS velocity profiles along the P1−P2 line, or parallel to the long axis of our FOV, and calculate the precession along the profile intersecting with the SMBH position. The method allows determination of the precession along strips parallel to this line. The precession along two strips on either side of the profile intersecting the SMBH position is also calculated, for a total of five determinations. The standard deviation is taken as the error. Using the best-fit value for θ_i, we derive $\Omega_P = -18 \pm 5 \, \mathrm{km \, s^{-1} \, pc^{-1}}$.

However, the original method by TW84 assumes that the disk is thin; the models from PT03 show that the best-fit disk is quite thick ($h/r \sim 0.4$). We check the results of the TW84 method by calculating the precession for the models of the same orientation as the best-fit model into which a known precession value has been injected. We find that the values obtained using the TW84 method for these models are

systematically too high. A line is fit to the output TW84 precessions to calibrate the method for the best-fit orientation. We extrapolate the fit to obtain the calibrated TW84 precession for our data: $62 \pm 5 \, \mathrm{km \, s^{-1} \, pc^{-1}}$. A model is generated using this precession, along with the best-fit orientation angles, and the goodness of fit to the data is calculated (Table 5); this precession gives a significantly worse fit to the data than the best-fit precession does, particularly to the velocity map. A comparison of the data and the models derived using the TW84 precession is shown in Appendix C.

6. Discussion

Chang et al. (2007) derived the maximum value for the precession of the eccentric disk, Ω_P, in order for gas released via stellar winds to end up on crossing orbits. Gas on these crossing orbits is able to collide, shock, cool, and fall into orbit around the SMBH on timescales faster than the viscous timescale. There, it collects into an accretion disk around P3 until it acquires enough mass to reach the Toomre instability limit and collapse to form stars. Based on a range of values for the disk thickness ($h/r = 0.1$–0.3), they calculated that the maximum precession that would allow these crossing orbits was $\Omega_P \lesssim 3$–$10 \, \mathrm{km \, s^{-1} \, pc^{-1}}$.
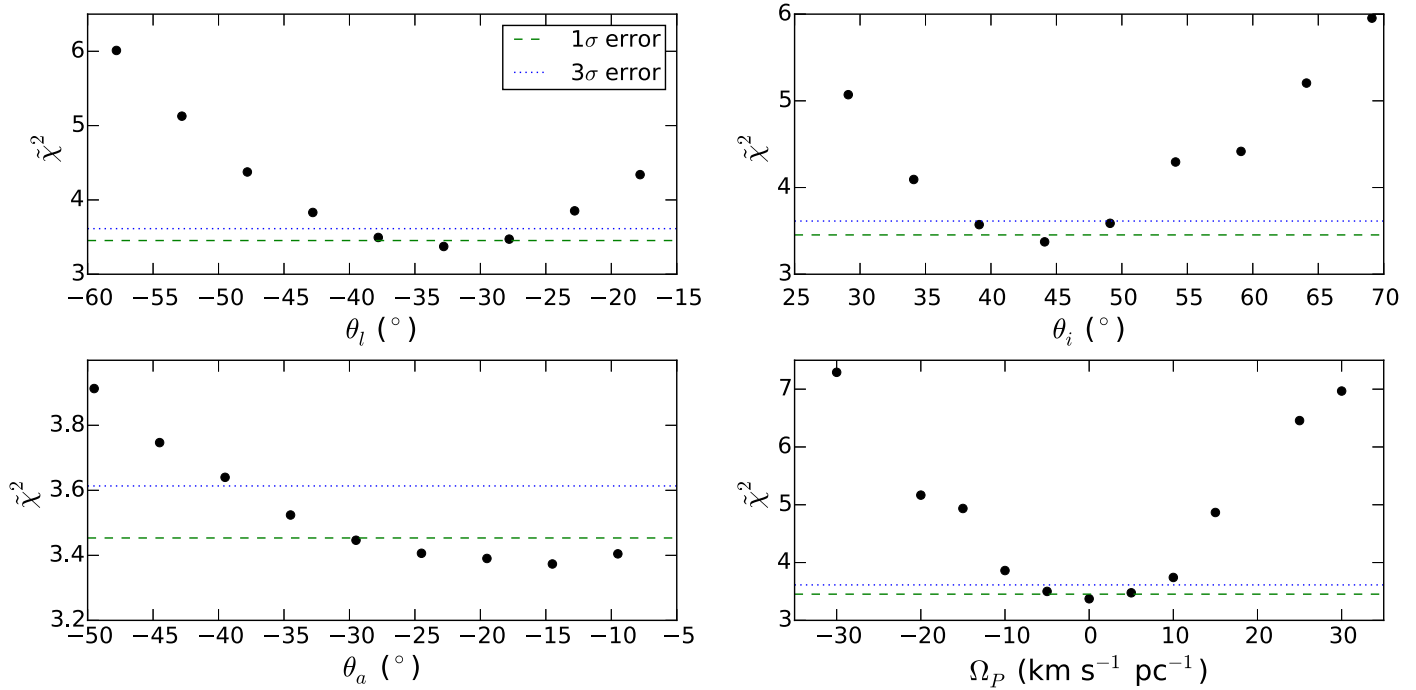
Figure 21. Reduced, weighted, and summed $\tilde{\chi}^2$ as a function of the four fitted parameters: θ_l, θ_i, θ_a, and Ω_P. For each, the three nonplotted parameters are held constant at their best-fit value, and only the given parameter is varied. The 1σ error, taken as the standard deviation of the minimum reduced, weighted, and summed $\tilde{\chi}^2$ from the MC simulations, is shown as the dashed horizontal line. The 3σ errors from the parameters are shown as the dotted horizontal lines.

Table 5
Minimum Reduced $\tilde{\chi}_m^2$ by Model

Moment	PT03	TW Ω_P	Best Fit per Moment	Total Best Fit
Flux	154.8	99.6	95.6	99.7
Velocity	21.9	190.8	11.3	14.1
Dispersion	4.0	3.6	3.1	3.3
$h3$[a]	13.2	11.6	7.7	9.5
$h4$[a]	8.2	7.4	6.5	6.9
Weighted total	4.7	18.9	...	3.4

Note.
[a] Not included in weighted fit.

The model fitting in Section 5.1 yielded a best-fit value for the precession equivalent to zero: $\Omega_P = 0.0 \pm 3.9$ km s^{-1} pc^{-1}. This is smaller than other values found for the precession of the disk (see Figure 25), but benefits from a combination of 2D FOV coverage and high spatial resolution unmatched by other observational studies. We note that there are many different modeling approaches in the literature and that our adopted models of PT03 have some limitations, which may impact the derived precession rate. Notably, the models do not include self-gravity (Peiris & Tremaine 2003, Section 5), nor do we include precession in a self-consistent fashion. However, the 3D SPH simulations of Hopkins & Quataert (2010), which include self-gravity and precession, also predict a slow (1–5 km s^{-1} pc^{-1}), rigid-body precession, in agreement with our results. Out of prior observational constraints on the precession, only B01 obtains a similarly small value of $\Omega_P = 3$ km s^{-1} pc^{-1} with their OASIS IFS data and 3D N-body modeling. Sambhus & Sridhar (2002) also fit their models to the IFS observations from B01 and obtain a higher

value of $\Omega_P = 16$ km s^{-1} pc^{-1}; however, they use Schwarzschild-type modeling and a thin-disk assumption.

Other modeling studies (Jacobs & Sellwood 2001; Salow & Statler 2001, 2004) have fit their models to long-slit spectroscopic data and obtain values of Ω_P ranging from 14 to over 30 km s^{-1} pc^{-1}. While several of the models used in these works include self-gravity (unlike PT03), they also assume a cold, thin disk, which may influence the derived precession rate. Sambhus & Sridhar (2000) use a modified Tremaine & Weinberg (1984) method with long-slit spectroscopy to estimate $\Omega_P \lesssim (\sin 77°/\sin i)\ 30$ km s^{-1} pc^{-1}. However, we found that this method produces precession values that are systematically offset from the known input model values, and hence this method appears to be unreliable for this system. Given the discrepancies between precession rates derived from different models and with new observational constraints from our data set, it is clear that further developments in dynamical models are needed.

Our best-fit precession is in line with the Chang et al. (2007) theory. The lack of precession in the eccentric disk allows gas released via stellar winds to quickly move into the vicinity of P3 and collect there, until enough gas has collected to collapse and form stars every 500 Myr.

Our best-fit disk orientation is tilted with respect to both the PT03 nonaligned orientation and the larger-scale galactic disk. It is more misaligned with the larger-scale galactic disk than was the PT03 nonaligned model. Examination of Figures 16 and 22 (right panel) shows that this is partly due to the differential morphology of the secondary brightness peak P2 in the NIR (see Appendix D for a comparison of the nonaligned models with the data they were fit to). In previous observations in the optical, the P.A. of a line connecting P1 and P2 is 43° (Lauer et al. 1993). However, in our NIR data, the P.A. of the P1−P2 line is aligned with the long axis of the OSIRIS FOV, or a P.A. of ∼56°. The angle θ_l has decreased compared to that
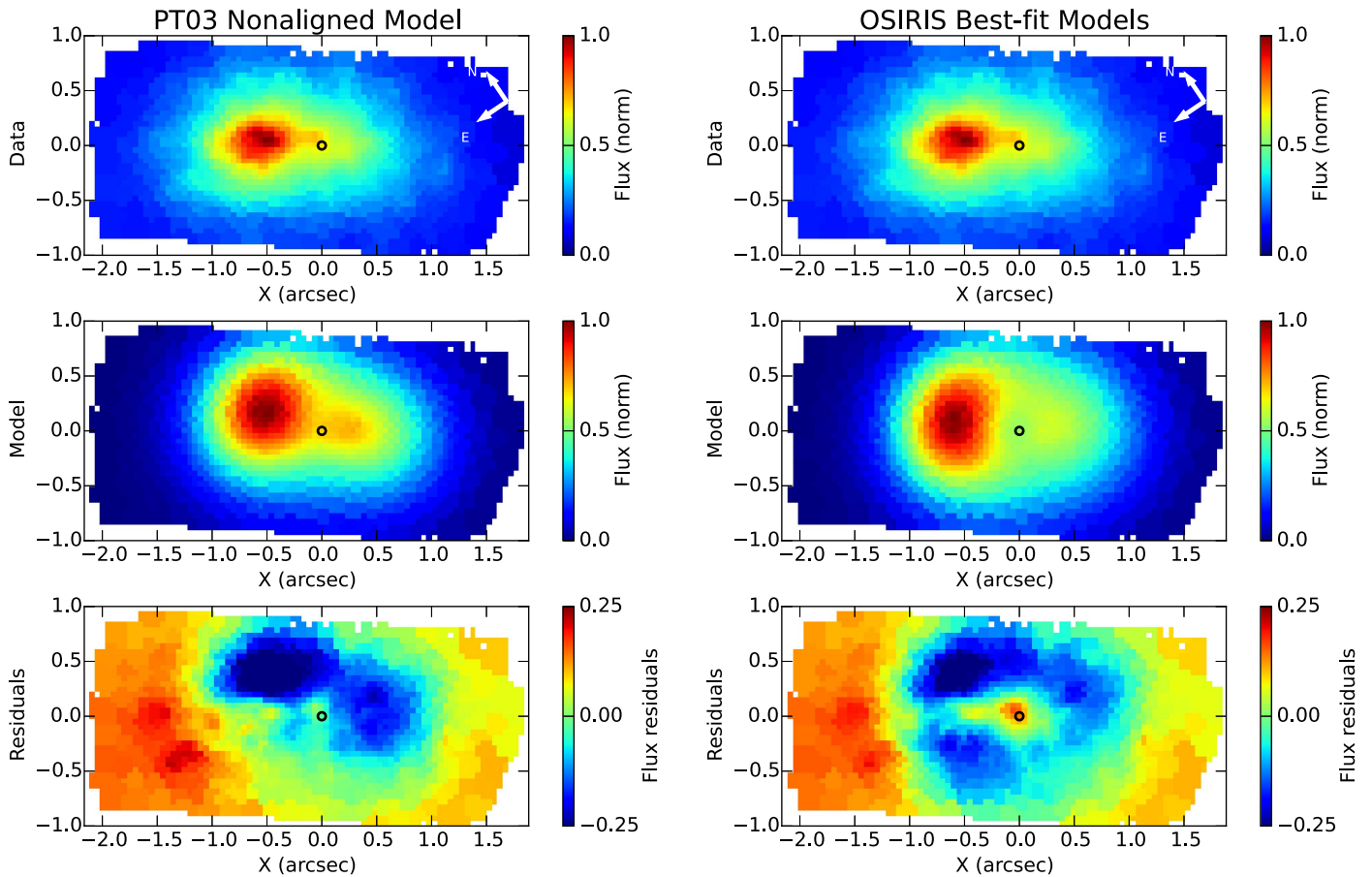
Figure 22. Comparison of data with modeled flux. The top panels show the normalized flux in the collapsed OSIRIS data cube, the middle panels show the modeled number of stars per spatial bin (normalized, taken to be equivalent to the flux), and the bottom panels show the residuals, data minus model. Left: comparison of data with nonaligned models from Peiris & Tremaine (2003). Right: comparison of data with best-fit models. Orientation angles and precession of the models are given in Table 6.

Table 6
Literature Parameters

Parameter	[1]	[2]	[3]	[4]	[5]	[6]	[7]
θ_l	...	$-48°$ [b]	...	...	$-27°34$ [b]	$-48°$ [a,b]	$-35°$
θ_i	$77°$ [a]	$55° \pm 5°$	...	$77°$ [a]	$51°54$	$52°5$	$57°$
θ_a [a]	...	...	$-21°$ [a,b]	...	...	...	$-34°$
Ω_P [c]	$\lesssim 47.7$ [d]	3	16	13.6	16	36.5	...

Notes.
[a] Assumed, from the literature.
[b] Converted from format given in literature.
[c] Units are km s^{-1} pc^{-1}.
[d] Given as a function of sin θ_i; adjusted to match our best-fit value.
References. [1] Sambhus & Sridhar 2000; [2] B01; [3] Jacobs & Sellwood 2001; [4] Salow & Statler 2001; [5] Sambhus & Sridhar 2002; [6] Salow & Statler 2004; [7] Brown & Magorrian 2013.

found by PT03 to compensate for this shift in morphology with wavelength. Our best-fit value for θ_l is more in line with that found by Brown & Magorrian (2013, $\theta_l = -35°$) in their modeling of the disk using observations from *HST*/WFPC2 (Lauer et al. 1998), *HST*/STIS (B05), and OASIS (B01) or by Sambhus & Sridhar (2002, $\theta_l = -27°34$) using the OASIS (B01) observations (see Table 6). In addition, the P1 peak is narrower and more elongated along the P1−P2 line in the NIR than in optical observations. The best-fit value for θ_i, which controls the inclination of the disk, is equivalent to a more face-on disk orientation than that of PT03 or other analyses in the

literature. The angle θ_a roughly controls the inclination of the disk along the minor axis and thus effectively adjusts the brightness at P1 and P2 to compensate for the change in the other angles. The source of the morphological differences between the optical and infrared is not understood; however, the 2D OSIRIS spectroscopy can be used to investigate the nature of the stellar populations in the eccentric disk.

The NIR data also allow insight into the distribution of the old stellar population in the nuclear region. Figure 7 shows that the UV-bright P3 gives way to a hole in the stellar distribution at redder wavelengths. This lack of cusp at the SMBH is similar
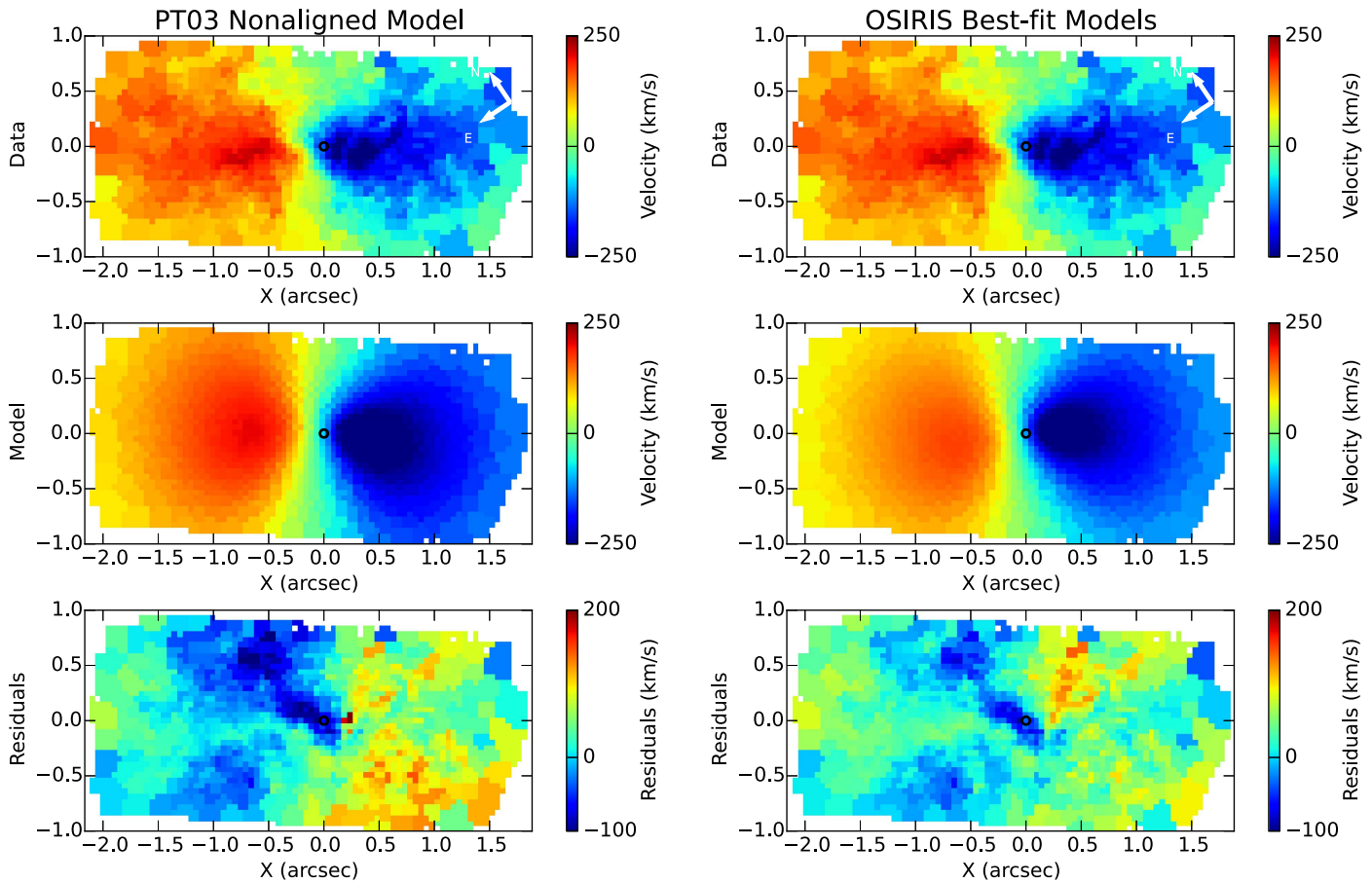
Figure 23. Comparison of OSIRIS velocity with modeled velocity. Panels are similar to those in Figure 22. Left: comparison of velocity data and PT03 nonaligned models. Right: comparison of velocity data and best-fit models.

to that seen in the Milky Way (Do et al. 2013). However, the inner core (or, potentially, hole) seen in the Milky Way's nuclear star cluster has a radius of at least 0.5 pc. At the distance of M31, this is equivalent to a core radius of 0″.13 on the sky, which is larger than that observed here (<0″.1). Future modeling efforts will aim to better model the size of the central hole in the stellar distribution in the NIR.

Previous high spatial resolution kinematics for this system were obtained using long-slit spectroscopy with *HST*. We find a similar kinematic structure to that seen in the STIS long-slit measurements from B05, though we note some discrepancies with our data, which may be attributable to different bulge subtraction methods. The previous highest spatial resolution kinematics with full 2D FOV coverage were limited by early-generation AO correction, and the resolution obtained, a factor of 4 poorer than that of the OSIRIS observations presented here, was a small improvement over seeing-limited observations. Comparison of the OASIS data from B01 with our OSIRIS kinematics, smoothed to their resolution, shows some discrepancies in alignment of the profiles, which may be attributable to differing SMBH positions. In addition, the dispersion peak reported by OASIS is much higher than that in our smoothed data; differing bulge subtraction methods may be the culprit. The results presented here show the value of the combination of the power of full 2D kinematic mapping with high spatial resolution and will be valuable for future modeling.

7. Conclusion

We present high-resolution, 2D kinematic maps of the nucleus of M31, enabling us to measure the orientation and precession rate of the eccentric disk of old stars. In comparison with previous *HST* optical images, the infrared data presented here show no signs of a central star cluster and rather show a hole in the infrared light at the black hole position. The 2D kinematics are largely in agreement with previous long-slit kinematic measurements. However, the new NIR flux maps favor a different orientation for the eccentric nuclear disk than the previous best-fit model fitted to optical data of Peiris & Tremaine (2003). The best-fit orientation for the morphology seen in the NIR is $[\theta_l, \theta_i, \theta_a] = [-33° \pm 4°, 44° \pm 2°, -15° \pm 15°]$, or offset from the best-fit model from Peiris & Tremaine (2003) by $[10°, -10°, 20°]$.

We also present a measurement of the precession rate for the eccentric disk of $\Omega_P = 0.0 \pm 3.9 \, \mathrm{km \, s^{-1} \, pc^{-1}}$. This slow precession rate favors the scenario put forth by Chang et al. (2007), suggesting that stellar winds from the AGB and red giant stars in the old eccentric disk provide the fuel for the starburst that produced the young nuclear cluster.
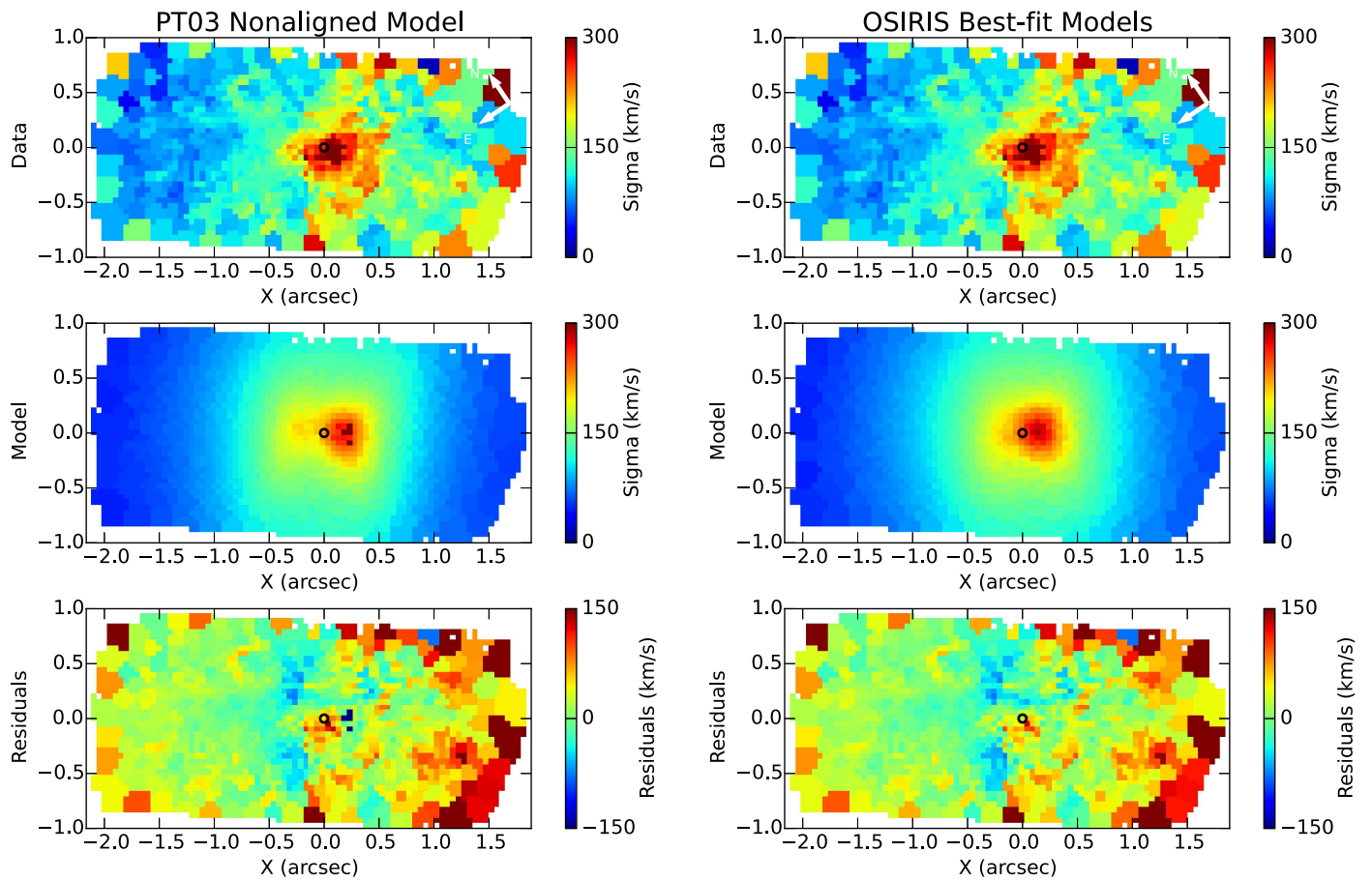
Figure 24. Comparison of OSIRIS dispersion with modeled dispersion. Panels are similar to those in Figure 22. Left: comparison of dispersion data and PT03 nonaligned models. Right: comparison of dispersion data and best-fit models.
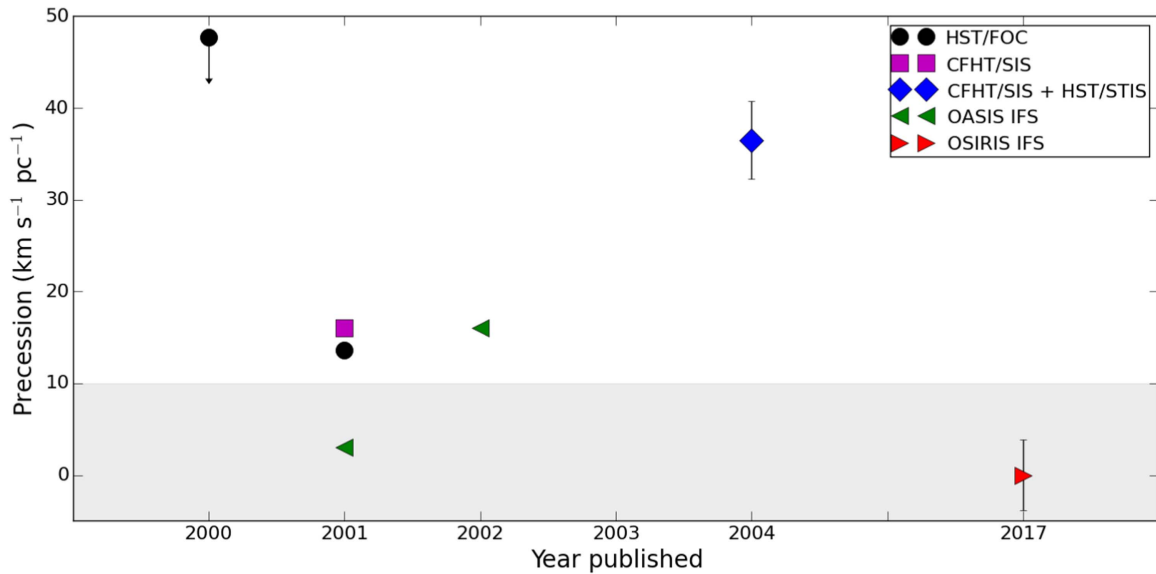
Figure 25. Previous estimates of the precession value of the eccentric disk, as a function of year published. Markers represent the source of the observations used in the analysis; all are long-slit observations except for the OASIS IFS green triangles and the red triangle, representing the current work. Error bars and upper limits are shown where provided in their respective papers. The precession value from Sambhus & Sridhar (2000) was given as a function of disk inclination and has been adjusted to match our best-fit disk inclination. The shaded gray box represents the theoretical limits from Chang et al. (2007).

Appendix A
Bulge Subtraction

Bulge subtraction is a critical aspect of the analysis, and in this appendix we explore the impact of different bulge subtraction approaches on the final kinematic fitting. First, we examine the pPXF fits for the spaxels determined to be bulge dominated; three representative spaxels are shown in Figure 26, along with their pPXF fits and the fit residuals. pPXF fits these non-bulge-subtracted spaxels well.

Second, we test our assumption that the outer portions of the data cube give a representative spectrum of the bulge. The family of best-fit templates was fairly uniform over the entire FOV. Figure 27 shows the best-fit intrinsic spectrum, before applying an LOSVD, for different bulge surface brightness ratios: the variation is minimal. Further, the broadband colors of the eccentric disk and the larger bulge have been shown to be identical (Saglia et al. 2010), suggesting that they contain the same population, with the exception of the more concentrated young nuclear cluster inside 0″.1.

Next, we explore the quality of our bulge subtraction in more detail by examining the correlation between the different velocity moments. Prior to bulge subtraction, there are strong correlations between h3 and the velocity as seen in the kinematic maps for the non-bulge-subtracted data, shown in Figure 28. This correlation is verified bin by bin in the left panel of Figure 29. Presumably, this effect comes from the fast disk rotation shifting absorption lines across the slowly rotating (or static, as we assume), unsubtracted bulge spectrum, which contributes a skewness to the resulting LOSVD. Interestingly, a
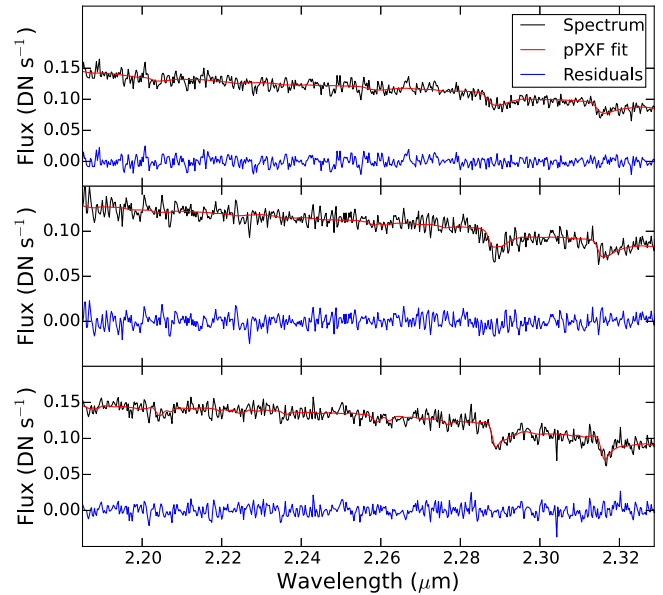

Figure 26. Spectra from three representative spaxels designated as bulge dominated, with the pPXF fits overlaid. Each spaxel is extracted from a different region of the FOV and all are shown before bulge subtraction. The pPXF fits, used to derive the bulge stellar, population as part of the bulge subtraction process, are shown in red for each spaxel. The residuals to the fits are shown in blue.

similar physical explanation produced an anticorrelation instead of a correlation between v and h3 in at least one other integral field data set for a different galaxy (Menezes et al. 2018). The correlations between the lower-order moments (v and σ) and the higher-order moments (h3 and h4) are also of great interest, as they can be interesting markers of other dynamical features such as bars (e.g., Iannuzzi & Athanassoula 2015). However, we believe that it is premature to use the higher-order moments h3 and h4 to draw scientific conclusions given their large error bars and systematic uncertainties (see Section 4.1 for details). Furthermore, after bulge subtraction, this correlation is largely removed as shown in the right panel of Figure 29.

Lastly, we test an extreme case of no bulge subtraction and explore the impact on the resulting disk orientation and precession speed. For the non-bulge-subtracted kinematic maps, the resulting best-fit inclination (θ_i) differs by 15°, going from 44° in the bulge-subtracted case to 29° in the non-bulge-subtracted case, which is a very significant change relative to the uncertainties (Table 6). The θ_a parameter changes from −14°.5 to −19°.5, within the uncertainties. There is no change in θ_l, and the precession rate changes from 0 to 5 km s^{-1} pc^{-1}, within the uncertainties. The $\tilde{\chi}^2$ is slightly higher in the non-bulge-subtracted case, going from 3.37 to 3.48. With the exception of the inclination, the final disk parameters are insensitive to errors in bulge subtraction.

The main conclusion of our tests is that bulge subtraction is essential; however, even in the most extreme case, the impact on the resulting disk properties is negligible, except for the inclination estimate.
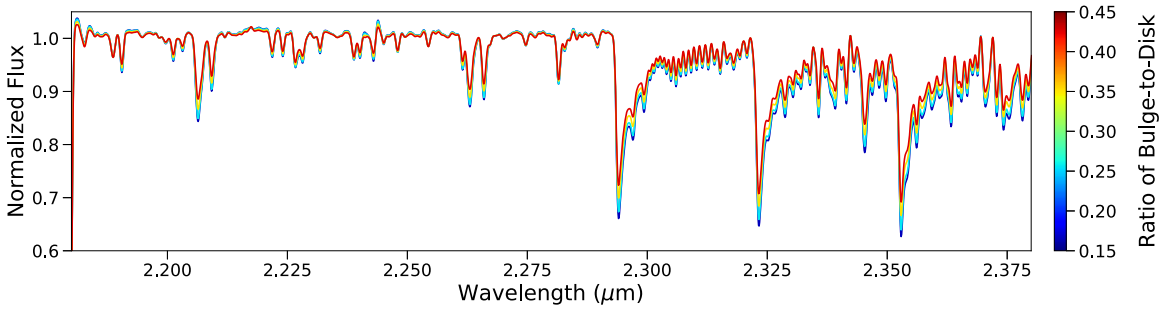
Figure 27. Composite spectral template, prior to convolution with the LOSVD, of spaxels with different bulge-to-disk ratios. The spectral template varies minimally between spaxels with different bulge contributions.
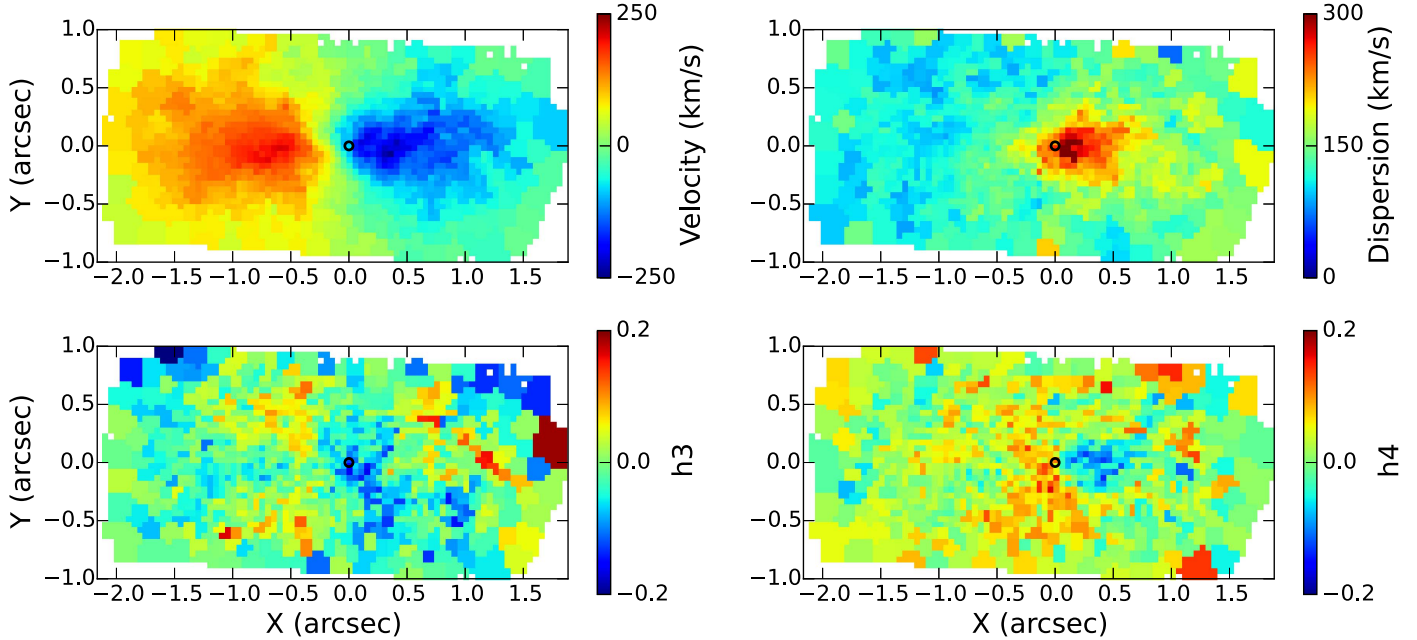
Figure 28. Kinematic maps, before bulge subtraction. The tessellation pattern is the same as that used for the bulge-subtracted data, for ease of comparison with Figure 12. While some correlations are present between the moments, the low S/N of $h3$ and $h4$ and the presence of systematic errors make it difficult to draw definitive conclusions from the higher-order moments.
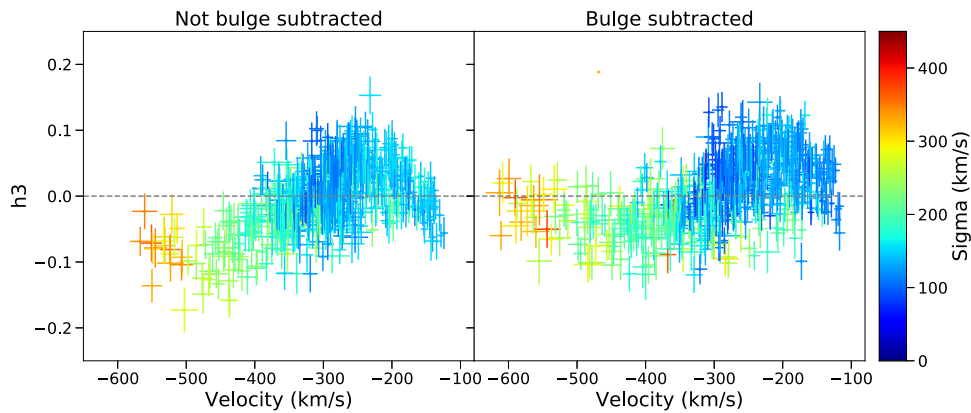

Figure 29. Correlations between $h3$ and velocity are strong before bulge subtraction (left) and decrease significantly after bulge subtraction (right). A similar correlation and improvement are also seen between $h3$ and the velocity dispersion, as shown in color.

Appendix B
SMBH Alignment Sources

P3, the compact young cluster assumed to be coincident with M31's SMBH, is bright in the UV but dark in the NIR.

Locating the SMBH in the OSIRIS data thus requires registering the UV and the NIR images. However, as there are essentially no compact sources bright in both bandpasses, we instead register pairs of frames adjacent in wavelength. We step through a total of eight frames, starting in the UV and
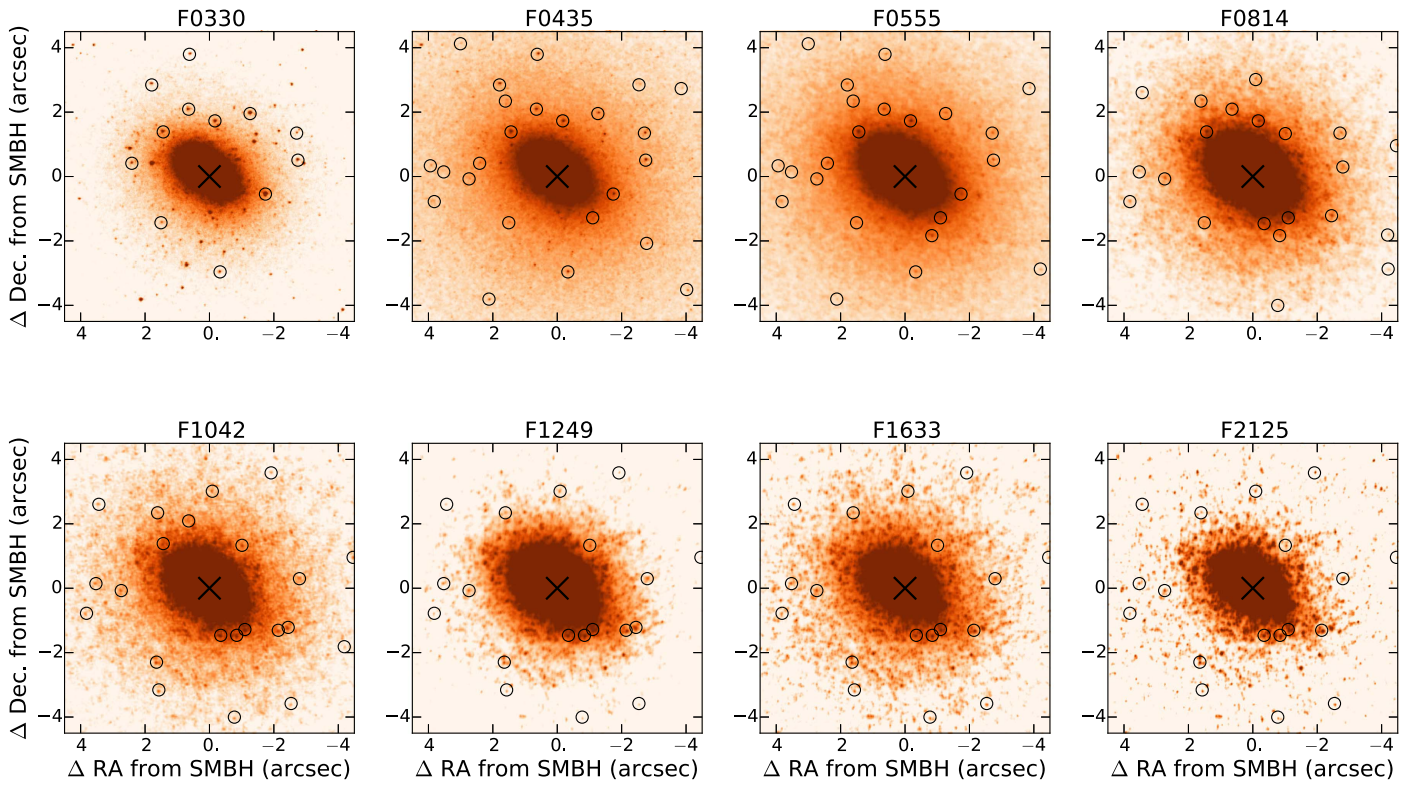
Figure 30. Images are aligned as in Section 3.4 and are shown scaled to match the F330W frame (pixel scale of $0\rlap{.}''025$ pixel^{-1}). The position of the SMBH is marked with the black cross and is accurate to $0\rlap{.}''033$ in the K$'$-band frame. The color scaling has been chosen to emphasize the faint outer region and the compact sources used for alignment. The alignment sources are circled in black.

ending in the NIR K' band. The alignment sources used are circled in Figure 30. The position of P3 is marked with a black cross, but as the color scaling is set to emphasize the fainter alignment sources, the inner nuclear disk structure is not visible in this figure.

Appendix C
TW Method Model Residuals

The precession of the eccentric disk is found using the method from Tremaine & Weinberg (1984), which only requires a 1D slice in both surface brightness and line-of-sight velocity. We show in Section 5.3 that this produces a value for the precession, $\Omega_P = 63.0 \pm 5.3$ km s^{-1} pc^{-1}, that is higher than that derived from the 2D model fitting. The goodness of fit is not improved for this value of the precession. Figure 31 shows the OSIRIS flux and kinematic maps compared to the models derived using the best-fit orientation and the precession from the TW84 method. While the flux and dispersion residuals are small, the velocity residuals are much higher than for the best-fit precession value of $\Omega_P = 0.0 \pm 3.9$ km s^{-1} pc^{-1}.
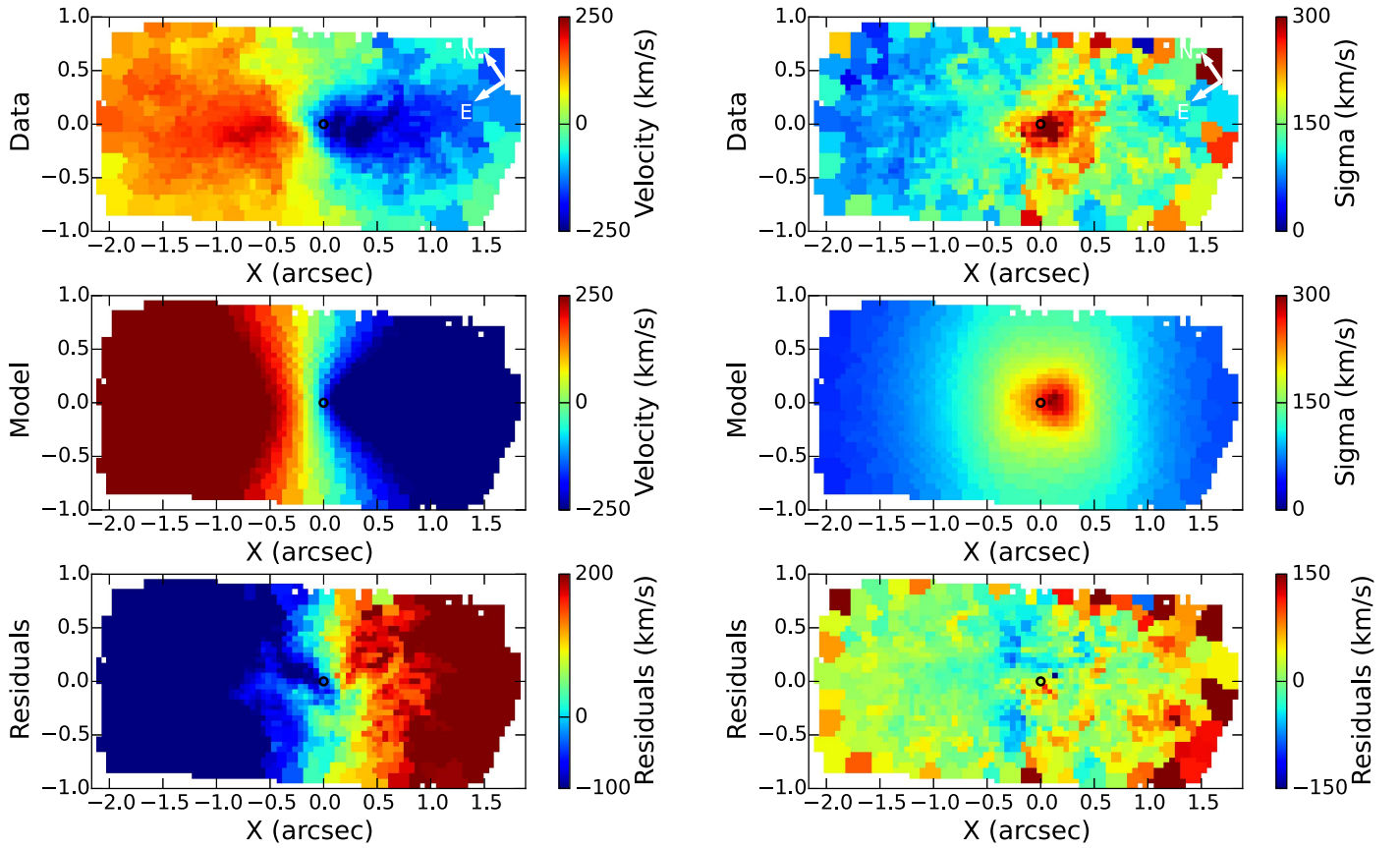
Figure 31. Comparison of OSIRIS data with the models suggested by the TW84 method. The orientation is the same as for our best-fit models, but the precession was derived using the TW84 method and calibrated using models with known precessions. While the dispersion residuals are small, the velocity residuals are much higher than with our best-fit precession value of 0 km s^{-1} pc^{-1}. The flux residuals are unchanged by the high precession and are identical to those in the right panel of Figure 22.

Appendix D
Nonaligned Model Residuals with *HST*/F555W Imaging

Lauer et al. (1998) observed the nuclear eccentric disk in M31 with *HST*/WFPC2 in the F300W, F555W, and F814W filters. We show the F555W image in Figure 32 (left panel). PT03 used this photometry, in combination with spectroscopy from KB99, to fit the orientation of their models. Their best-fit models to the data are not aligned with the larger-scale galactic disk of M31 and are designated as the nonaligned models (Table 6). Figure 32 shows the nonaligned models and the residuals between the F555W photometry and these models. Comparison of this figure with Figure 22 shows that while the nonaligned models are a good fit to the F555W photometry, they are not a good fit to the OSIRIS NIR photometry.
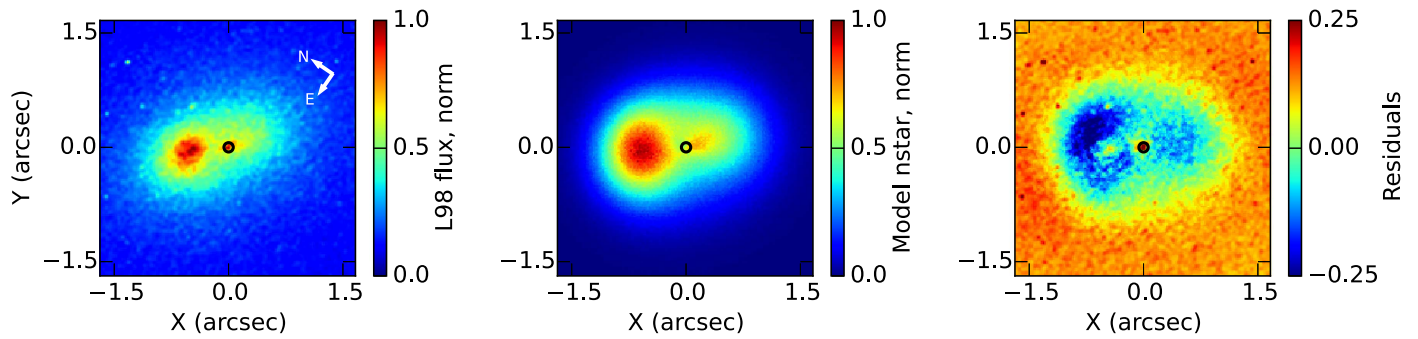
Figure 32. Comparison of F555W flux map from Lauer et al. (1998) with the nonaligned models from PT03. These photometric data were used for the fitting of the original models. In all, the SMBH position is marked with the black circle and the P.A. = 55°.7, the original P.A. from Lauer et al. (1998) (note that this P.A. differs from that of the OSIRIS figures). Left: F555W flux map, scaled so the peak flux is equal to 1. Middle: modeled number of stars per spatial bin, binned to the subsampled F555W pixel scale of $0''0228$ pixel^{-1}. The models are oriented using the nonaligned orientation from PT03 (angles given in Table 6) and scaled so the peak is equal to 1. Right: residuals, data minus models.

ORCID iDs

K. E. Lockhart ⓘ https://orcid.org/0000-0002-8130-1440
J. R. Lu ⓘ https://orcid.org/0000-0001-9611-0009
H. V. Peiris ⓘ https://orcid.org/0000-0002-2519-584X
A. M. Ghez ⓘ https://orcid.org/0000-0003-3230-5055

References

Allen, D. A., Hyland, A. R., & Hillier, D. J. 1990, MNRAS, 244, 706
Bacon, R., Emsellem, E., Combes, F., et al. 2001, A&A, 371, 409
Battistini, P. L., Bonoli, F., Casavecchia, M., et al. 1993, A&A, 272, 77
Bender, R., Kormendy, J., Bower, G., et al. 2005, ApJ, 631, 280
Brown, C. K., & Magorrian, J. 2013, MNRAS, 431, 80
Cappellari, M., & Copin, Y. 2003, MNRAS, 342, 345
Cappellari, M., & Emsellem, E. 2004, PASP, 116, 138
Chang, P., Murray-Clay, R., Chiang, E., & Quataert, E. 2007, ApJ, 668, 236
Courteau, S., Widrow, L. M., McDonald, M., et al. 2011, ApJ, 739, 20
Do, T., Martinez, G. D., Yelda, S., et al. 2013, ApJL, 779, L6
Dorman, C. E., Widrow, L. M., Guhathakurta, P., et al. 2013, ApJ, 779, 103
Galleti, S., Bellazzini, M., Federici, L., Buzzoni, A., & Fusi Pecci, F. 2007, A&A, 471, 127
Genzel, R., Crawford, M. K., Townes, C. H., & Watson, D. M. 1985, ApJ, 297, 766
Goodman, J. 2003, MNRAS, 339, 937
Hanson, M. M., Conti, P. S., & Rieke, M. J. 1996, ApJS, 107, 281
Hopkins, P. F., & Quataert, E. 2010, MNRAS, 405, L41
Iannuzzi, F., & Athanassoula, E. 2015, MNRAS, 450, 2514
Jacobs, V., & Sellwood, J. A. 2001, ApJL, 555, L25
Kausch, W., Noll, S., Smette, A., et al. 2015, A&A, 576, A78
Kazandjian, M. V., & Touma, J. R. 2013, MNRAS, 430, 2732
Kolykhalov, P. I., & Syunyaev, R. A. 1980, SvAL, 6, 357
Kormendy, J., & Bender, R. 1999, ApJ, 522, 772
Krabbe, A., Gasaway, T., Song, I., et al. 2004, Proc. SPIE, 5492, 1403
Larkin, J., Barczys, M., Krabbe, A., et al. 2006, Proc. SPIE, 6269, 62691A
Lauer, T. R., Bender, R., Kormendy, J., Rosenfield, P., & Green, R. F. 2012, ApJ, 745, 121
Lauer, T. R., Faber, S. M., Ajhar, E. A., Grillmair, C. J., & Scowen, P. A. 1998, AJ, 116, 2263

Lauer, T. R., Faber, S. M., Groth, E. J., et al. 1993, AJ, 106, 1436
Levin, Y., & Beloborodov, A. M. 2003, ApJL, 590, L33
Livingston, W., & Wallace, L. 1991, An Atlas of the Solar Spectrum in the Infrared from 1850 to 9000 cm-1 (1.1 to 5.4 micrometer) (Tucson, AZ: National Solar Observatory)
Lu, J. R., Ghez, A. M., Hornstein, S. D., et al. 2009, ApJ, 690, 1463
Maiolino, R., Rieke, G. H., & Rieke, M. J. 1996, AJ, 111, 537
McConnachie, A. W., Irwin, M. J., Ferguson, A. M. N., et al. 2005, MNRAS, 356, 979
McConnell, N. J., Lu, J. R., & Mann, A. W. 2015, arXiv:1506.07880
Melchior, A.-L., & Combes, F. 2013, A&A, 549, A27
Menezes, R. B., da Silva, P., & Steiner, J. E. 2018, MNRAS, 473, 2198
Menezes, R. B., Steiner, J. E., & Ricci, T. V. 2013, ApJL, 762, L29
Morris, M. 1993, ApJ, 408, 496
Nieten, C., Neininger, N., Guélin, M., et al. 2006, A&A, 453, 459
Olsen, K. A. G., Blum, R. D., Stephens, A. W., et al. 2006, AJ, 132, 271
Paumard, T., Genzel, R., Martins, F., et al. 2006, ApJ, 643, 1011
Peiris, H. V., & Tremaine, S. 2003, ApJ, 599, 237
Rich, R. M., Mighell, K. J., Freedman, W. L., & Neill, J. D. 1996, AJ, 111, 768
Rossa, J., van der Marel, R. P., Böker, T., et al. 2006, AJ, 132, 1074
Saglia, R. P., Fabricius, M., Bender, R., et al. 2010, A&A, 509, A61
Salow, R. M., & Statler, T. S. 2001, ApJL, 551, L49
Salow, R. M., & Statler, T. S. 2004, ApJ, 611, 245
Sambhus, N., & Sridhar, S. 2000, ApJL, 539, L17
Sambhus, N., & Sridhar, S. 2002, A&A, 388, 766
Sanders, R. H. 1992, Natur, 359, 131
Seth, A. C., Dalcanton, J. J., Hodge, P. W., & Debattista, V. P. 2006, AJ, 132, 2539
Smette, A., Sana, H., Noll, S., et al. 2015, A&A, 576, A77
Sofue, Y., & Yoshida, S. 1993, ApJL, 417, L63
Statler, T. S., King, I. R., Crane, P., & Jedrzejewski, R. I. 1999, AJ, 117, 894
Tremaine, S. 1995, AJ, 110, 628
Tremaine, S., & Weinberg, M. D. 1984, ApJL, 282, L5
van Dam, M. A., Bouchez, A. H., Le Mignant, D., et al. 2006, PASP, 118, 310
van der Marel, R. P., & Franx, M. 1993, ApJ, 407, 525
Winge, C., Riffel, R. A., & Storchi-Bergmann, T. 2009, ApJS, 185, 186
Wizinowich, P. L., Le Mignant, D., Bouchez, A. H., et al. 2006, PASP, 118, 297
Yelda, S., Ghez, A. M., Lu, J. R., et al. 2014, ApJ, 783, 131